Article

Li metal deposition and stripping in a solid-state battery via Coble creep

https://doi.org/10.1038/s41586-020-1972-y

Received: 4 May 2018

Accepted: 1 November 2019

Published online: 3 February 2020

Yuming Chen[1,2,3,10], Ziqiang Wang[1,2,10], Xiaoyan Li[1,2,3,4], Xiahui Yao[1,2], Chao Wang[1,2], Yutao Li[5,6], Weijiang Xue[1,2], Daiwei Yu[7], So Yeon Kim[1,2], Fei Yang[1,2], Akihiro Kushima[8], Guoge Zhang[4], Haitao Huang[4], Nan Wu[5,6], Yiu-Wing Mai[9], John B. Goodenough[5,6] & Ju Li[1,2]*

Solid-state lithium metal batteries require accommodation of electrochemically generated mechanical stress inside the lithium: this stress can be[1,2] up to 1 gigapascal for an overpotential of 135 millivolts. Maintaining the mechanical and electrochemical stability of the solid structure despite physical contact with moving corrosive lithium metal is a demanding requirement. Using in situ transmission electron microscopy, we investigated the deposition and stripping of metallic lithium or sodium held within a large number of parallel hollow tubules made of a mixed ionic-electronic conductor (MIEC). Here we show that these alkali metals—as single crystals—can grow out of and retract inside the tubules via mainly diffusional Coble creep along the MIEC/metal phase boundary. Unlike solid electrolytes, many MIECs are electrochemically stable in contact with lithium (that is, there is a direct tie-line to metallic lithium on the equilibrium phase diagram), so this Coble creep mechanism can effectively relieve stress, maintain electronic and ionic contacts, eliminate solid-electrolyte interphase debris, and allow the reversible deposition/stripping of lithium across a distance of 10 micrometres for 100 cycles. A centimetre-wide full cell—consisting of approximately 10^{10} MIEC cylinders/solid electrolyte/$LiFePO_4$—shows a high capacity of about 164 milliampere hours per gram of $LiFePO_4$, and almost no degradation for over 50 cycles, starting with a 1× excess of Li. Modelling shows that the design is insensitive to MIEC material choice with channels about 100 nanometres wide and 10–100 micrometres deep. The behaviour of lithium metal within the MIEC channels suggests that the chemical and mechanical stability issues with the metal–electrolyte interface in solid-state lithium metal batteries can be overcome using this architecture.

Demands for safe, dense energy storage provide incentive for the development of all-solid-state rechargeable Li metal batteries[3–5]. (Lithium metal batteries are to be distinguished from lithium ion batteries, in which the anode does not contain metallic lithium.) Lithium in the body-centred cubic (b.c.c.) crystal structure has 10× the gravimetric capacity and 3× the volumetric capacity of graphite[6]. The problem is that the non-lithium-metal volume fraction ϕ, consisting of entrapped solid-electrolyte interphase (SEI) debris, pores and other ancillary/host structures, tends to increase with battery cycling[7–12]. Once a Li-metal-containing anode has $\phi > 70\%$, it loses its volumetric advantage compared to a graphite anode. Most solid electrolytes are thermodynamically unstable in contact with the corrosive Li metal[13], forming SEI at a fresh solid electrolyte/Li metal interface. This thermodynamic instability can be predicted by checking the equilibrium phase diagram: it occurs when the solid electrolyte phase does not have a direct tie-line connecting to the Li_{bcc} phase. Ab initio calculations have shown that a small number of compounds such as LiF, LiCl and Li_2O are absolutely stable against Li metal, but they are poor ionic conductors[13]. Good solid electrolytes (ionic conductors but electronic insulators) will decompose upon contact with Li_{bcc} to form SEI. Under large fluctuating mechanical stresses the SEI and the solid electrolyte can spall off and get entangled with Li: and as they are electronic insulators, they can cut off electronic percolation and cause 'dead lithium'. The dual requirements of maintaining contact and adhesion with moving Li without fracture (mechanical stability) while reducing SEI production (electrochemical stability) makes the problem hard from an electrochemo-mechanics perspective.

Metallic lithium has a volume $\Omega = 21.6\ Å^3$ per atom = 0.135 eV per GPa. This means that an overpotential U of −0.135 V, which is frequently seen experimentally in Li deposition, can in principle generate GPa-level

[1]Department of Nuclear Science and Engineering, Massachusetts Institute of Technology, Cambridge, MA, USA. [2]Department of Materials Science and Engineering, Massachusetts Institute of Technology, Cambridge, MA, USA. [3]College of Environmental Science and Engineering, Fujian Normal University, Fuzhou, China. [4]Department of Applied Physics, The Hong Kong Polytechnic University, Hong Kong, China. [5]Texas Materials Institute, The University of Texas at Austin, Austin, TX, USA. [6]Materials Science and Engineering Program, The University of Texas at Austin, Austin, TX, USA. [7]Department of Electrical Engineering and Computer Science, Massachusetts Institute of Technology, Cambridge, MA, USA. [8]Advanced Materials Processing and Analysis Center, Department of Materials Science and Engineering, University of Central Florida, Orlando, FL, USA. [9]Centre for Advanced Materials Technology (CAMT), School of Aerospace, Mechanical and Mechatronics Engineering, The University of Sydney, Sydney, New South Wales, Australia. [10]These authors contributed equally: Yuming Chen, Ziqiang Wang. *e-mail: liju@mit.edu

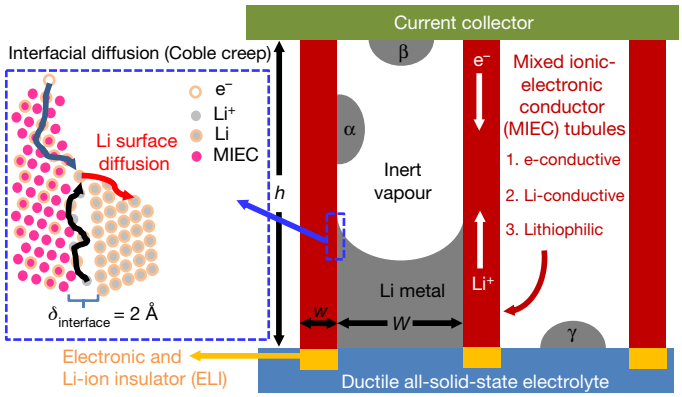

Fig. 1 | Mixed ionic-electronic conductor (MIEC) tubules as 3D Li hosts. Schematic process of creep-enabled Li deposition/stripping in an MIEC tubular matrix with a geometry of {h, W, w}, where Coble creep dominates via interfacial diffusion along the MIEC/Li_{bcc} incoherent interface. Main panel, cross-section of the matrix: MIEC tubules are shown as red, with white arrows indicating the free movements of electrons (e^-) and lithium ions (Li^+); the three required properties of the MIEC (red arrow) are labelled 1, 2 and 3. An electronic and Li-ion insulator (ELI: yellow) material is used at the root of the MIEC as a 'binder' to the solid electrolyte ('Ductile all-solid-state electrolyte'). α, β and γ are Li_{bcc} drops that are still recoverable. The boxed area is shown expanded in the inset: see Methods section 'Quantitative analysis' for details.

hydrostatic pressure ($P_{LiMetal}$) in Li according to the Nernst equation[2,14], and this stress will be transmitted to the surrounding solid structure. If these electrochemically generated mechanical stresses are not relieved, Li fingers or wedges may crack the solid electrolyte[2], through its grain boundaries or through its lattice. As the crack tip may be closer to the cathode, there is a transport advantage to the deposition of more Li at the crack tip, so $P_{LiMetal}(\mathbf{x})$ is generated again at the crack tip where $\mathbf{x}$ is spatial position, and the process repeats until electrical shorting happens[1]. The well-known elastic-modulus-based criterion[5] for mechanical stability is not applicable when considering this crack-based degradation mode. The potentially huge electrochemically generated stress $P_{LiMetal}(\mathbf{x})$, if not relaxed quickly by creeping of Li, would fracture solid components. This and the chemical attack leading to SEI production makes the architecture of all-solid-state rechargeable Li metal batteries difficult to construct, even at a conceptual level.

Because Li melts at $T_M = 180$ °C and is a soft metal, an alternative concept is to have the Li flow into and out of a 3D tubular structure like that shown in Fig. 1[15–17], keeping contact with a 3D solid host structure made of mixed ionic-electronic conductor (MIEC) that is absolutely electrochemically stable against Li metal (that is, having a direct tie-line to Li_{bcc} phase on the equilibrium phase diagram without intervening phases). Such 3D host structures have been studied experimentally in the past[15–17], but here we seek quantitative mechanistic understanding for the plating/stripping behaviour. We note that, in our construction, we choose only the MIEC (not the solid electrolyte) to be in thermodynamic equilibrium with Li, so it will not generate any SEI upon contact with Li, removing the possibility of SEI and SEI-based degradation. At 300 K, the homologous temperature for Li is $T/T_M = 0.66$, so Li should manifest an appreciable creep strain rate $\dot{\varepsilon}(T, \sigma)$ (where σ is the deviatoric shear stress) by dislocation power-law creep or diffusional creep mechanisms, according to the deformation mechanism map of metals[18,19]. Creep imparts an effective viscosity $\eta \equiv \sigma/\dot{\varepsilon}(T, \sigma)$, so the Li may behave like an 'incompressible work fluid', and advancement and retraction of pure Li may be established inside the MIEC tubules (which cannot chemically react with the corrosive work fluid), driven by the chemical potential/pressure gradient $-\Omega\nabla P_{LiMetal}(\mathbf{x})$. The competition between interfacial-diffusional Coble creep, bulk diffusional Nabarro–Herring creep, and hybrid diffusive-displacive dislocation creep mechanisms depends on the grain size. The pore space helps to relieve the stresses (hydrostatic and deviatoric) by allowing the Li_{bcc} to backfill by diffusion, so the all-solid-state host is not fractured during cycling (ensuring mechanical stability), while maintaining high-quality electronic and ionic contacts. While few solid electrolytes with satisfactory Li-ion conductivity are electrochemically stable against Li_{bcc} (ref. [13]), there exist many MIECs with such stability and they will not decompose to form fresh SEI at the MIEC/metal interface. These include popular anode materials like lithiated graphite or hard carbon (LiC_6 is an MIEC), Si ($Li_{22}Si_5$ is an MIEC), Al (Li_9Al_4 is an MIEC) and so on[20], as well as materials with appreciable solubility of Li atoms as a random solid solution ($CuLi_x$) or even bulk-immiscible metals (such as M = Ni, W) that may nonetheless support some Li solubility at the M/Li_{bcc} phase boundary. Here we focus on lithiated carbonaceous materials as the MIEC 'rail' that guides Li_{bcc} deposition and stripping, although in the 'Quantitative analysis' section of Methods we show that this design is almost independent of MIEC material when using channels about 100 nm wide and 10–100 μm deep.

The cycling of Li under alternating negative and positive overpotential is rather like the application of a pump, which can produce fatigue in the solid host structure. To avoid such fatigue, the MIEC walls should be sufficiently strong and ductile to accommodate the stresses generated by $P_{LiMetal}$ and capillarity. Typical graphene foam with too thin a wall thickness w may not be appropriate because such walls may easily tear, crumble or fold due to van der Waals adhesion. Also, the contact condition between the MIEC and the solid electrolyte capping layer is important, as this is where Li deposition is most likely to occur initially and where $P_{LiMetal}$ is initiated. A root or coating of an electronic and Li-ion insulator (ELI) material like BeO, SrF_2 or AlN (with a bandgap >4.0 eV, and thermodynamically stable against Li_{bcc}) might be used to bind the MIEC to the solid electrolyte. A mechanically compliant solid electrolyte, for example polyethylene oxide (PEO), could be used to prevent the brittle root-fracture problem.

In the following experiments, we use lithiated carbon tubules ~100 nm wide as the MIEC material. We demonstrate plating/stripping of Li or Na inside individual carbon tubules in an in situ transmission electron microscope (TEM) experiment, where a PEO-based polymer about 50 μm thick was used as the solid electrolyte. The opposite side of the solid electrolyte was coated with a Li counter-electrode connected to the scanning tunnelling microscope (STM)/TEM manipulator. The TEM copper grid (Fig. 2a and Supplementary Fig. 1) serves as the current collector attached to the carbon tubules on the other end. The carbon tubule has an inner diameter W of around 100 nm, and its walls of width $w \approx 20$ nm are also nanoporous, as shown in Fig. 2b and Supplementary Fig. 2a, b[21].

Figure 2b–d shows TEM images of the Li plating process in a single carbon tubule with ZnO_x as a lithiophilic agent introduced by controlling the synthetic process (see Methods and Supplementary Video 1). Figure 2e, f and Supplementary Video 2 show the changes of selected-area electron diffraction (SAED) patterns when deposited Li passes through the original void. After the ring pattern of the carbon tubule and a period of changing SAED patterns, the SAED (Fig. 2f) stays stable and shows a strong texture: $(110)_{Li\,bcc} \perp$ tubule axis and $(1\bar{1}0)_{Li\,bcc} //$ tubule axis (Supplementary Fig. 3 also demonstrates the single-crystal feature). Moreover, a high-resolution TEM (HRTEM) video captures the first appearance of the fresh Li crystal, with a 0.248-nm lattice spacing measured between (110) crystal planes perpendicular to the wall (Fig. 2g–i and Supplementary Video 3). We decreased the electron beam current to 0.3 A cm^{-2} to maintain the HRTEM image of the Li crystal for several seconds. The Li can also be stripped along the tubule (Supplementary Fig. 4) by retracting the Li_{bcc} tip. The tip can plate and strip a length of more than 6 μm along the carbon tubule, which was the largest unblocked length of carbon tubule we could find (Supplementary Figs. 5 and 6). It can even climb over partial obstructions inside the carbon tubule (Supplementary Fig. 7). We also discovered

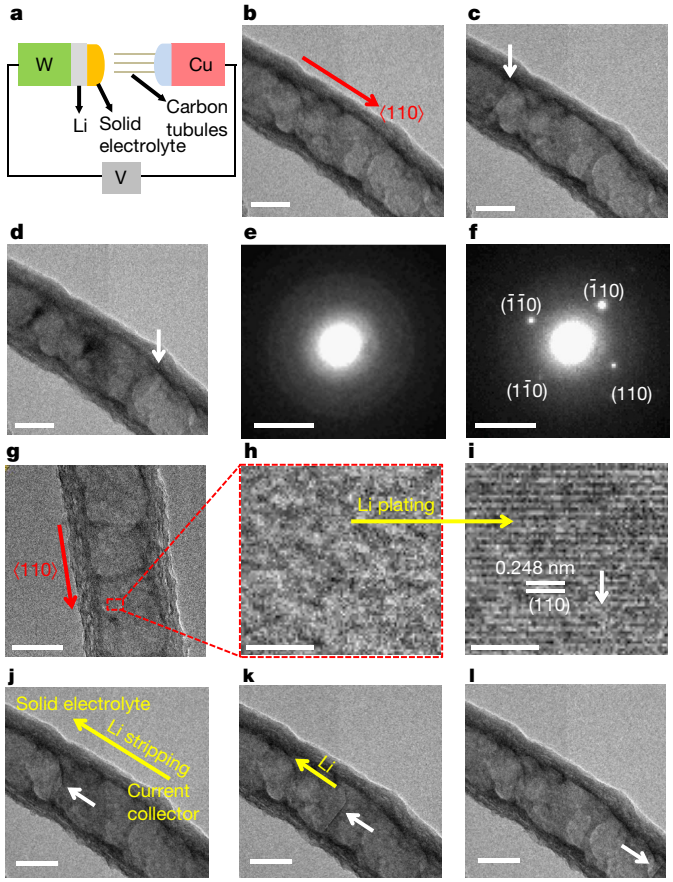

Fig. 2 | Lithium plating/stripping inside carbon tubules. a, In situ TEM set-up: see Methods for details. **b**–**d**, TEM imaging of Li plating with fronts marked by white arrows (Supplementary Video 1) at increasing time. **e**, **f**, SAED changes from **e** to **f** during Li plating (Supplementary Video 2). **g**–**i**, HRTEM imaging of a tubule before plating (**g**; boxed region shown magnified in **h**) and after plating (**i**, showing first formation of a Li crystal (Supplementary Video 3)). The red arrow indicates the Li atomic transport direction in deposition, pointing from the solid-electrolyte to the current collector. **j**–**l**, TEM imaging of Li stripping with a void plug between Li and solid electrolyte, with the Li atomic transport direction indicated by the yellow arrow (from current-collector side to the solid-electrolyte side), and the surface extent indicated by white arrows (Supplementary Video 4). Scale bars: **b**–**d**, **g**, **j**–**l**, 100 nm; **h**, **i**, 2 nm; and **e**, **f**, 5 nm^{-1}.

reversible Li plating/stripping in aligned double carbon tubules (Supplementary Fig. 8 and Supplementary Video 5). The lithium filling ratio inside the tubule was estimated by electron energy-loss spectroscopy (EELS) thickness measurement. The Li K-edge of EELS (Supplementary Fig. 8c, d) is observed after Li plating at the location shown by a red cross in Supplementary Fig. 8a[7,22]. The diameter of the plated Li_{bcc} plug is estimated to be 92 nm, which can be compared to the inner diameter of the tubule, about 100 nm. Li_{bcc} can also be plated in three aligned tubules simultaneously (Supplementary Fig. 9).

We have tested the cycling stability of the carbonaceous MIEC tubules by in situ TEM, and found they can maintain excellent structural integrity even after 100 cycles of Li plating and stripping (Supplementary Video 6, Supplementary Figs. 10, 11). Li can also plate/strip inside tubules of different sizes, and even within tubules filled with 3D obstacles (Supplementary Figs. 7, 12–14). Our observations indicate that the internal Li shape change is not displacive/convective, but rather a diffusive plating/stripping process onto a front or fronts, which is much more tolerant of internal obstructions or obstacles. Similar results for plating/stripping sodium metal are shown in Supplementary Figs. 15, 16 and Supplementary Videos 7, 8.

When stripping Li (Supplementary Video 4, Fig. 2j–l and Supplementary Fig. 17), we can sometimes create a void plug that grows between the residual Li and the solid electrolyte. Yet this gap does not prevent the Li from being further stripped, growing the void that separates the solid electrolyte from residual lithium. Lithium must therefore be extracted from the wall or surface of the MIEC. This excludes dislocation power-law creep as a major kinetic mechanism, since dislocation slip cannot occur in the void, and the residual Li shows little mechanical translation (convection) in our experiments, although slight local sliding cannot be excluded. Therefore, dislocation creep is not the dominant creep mechanism.

To determine the dominant mechanism of Li plating/stripping in MIEC tubules —either interfacial-diffusional Coble creep or bulk diffusional Nabarro–Herring creep—we carried out theoretical calculations (see Methods section 'Quantitative analysis'). We considered three possible paths for Li diffusion: (a) via an MIEC wall of width w (~10 nm); (b) via the interface between an MIEC wall and Li_{bcc}, with an atomic width of $\delta_{interface}$ (~2 Å); and (c) via bulk Li_{bcc} of width W (~100 nm). We also considered three canonical MIECs—LiC_6, $Li_{22}Si_5$ and Li_9Al_4. Generally, for the cases when an MIEC is thermodynamically stable against Li_{bcc}, the calculations show that Li diffusion via the interfacial path (b) dominates. This means that the MIEC tubule concept is feasible for Li_9Al_4 and $Li_{22}Si_5$—or any other electrochemically stable MIEC (for example, $CuLi_x$, Ni, W) that forms an incoherent interface with Li_{bcc}. In all such cases, the diffusion flux along the 2-Å incoherent interface between the MIEC and the metal, or over the MIEC surface, dominates over flux through the 10-nm MIEC wall itself. In other words, ion transport along the MIEC is dominated by the 2-Å 'interfacial MIEC channel', as illustrated in Fig. 1. This greatly widens the range of material choices available for the MIEC, as we can now separate its mechanical function from its electron/ion-transport functions.

Because carbon needs to be lithiated to LiC_6 to become a true MIEC, we introduced ZnO_x during synthesis of the carbon tubules to improve their lithiophilicity, which greatly helps the achievement of uniform-quality MIEC tubules on the first lithiation. We now consider the mechanism of ZnO_x-induced lithiophilicity[23,24]. On first lithiation, ZnO_x in the MIEC undergoes a conversion/alloying reaction to produce Li_2O, as follows[25]: $ZnO_x + (2x + y)Li = ZnLi_y + xLi_2O$. But it is experimentally difficult to obtain TEM images of the post-formation Li_2O directly: the material is only a few nanometres thick, and located on the inner surfaces of the carbon tubules. We used an alternative method to observe the in situ formed Li_2O, namely imaging the outer surface of the carbon tubules, taking advantage of the homogeneous distribution of ZnO_x across the carbon tubule wall (Supplementary Fig. 2). During Li plating, a crystalline Li_2O layer with a thickness of a few nanometres is observed to be formed along the outer surface of the carbon tubule (Fig. 3a and Supplementary Fig. 18) like a lubricant. Li_2O seems to be mechanically soft, despite its crystallinity, and can also deform by diffusional creep, even at room temperature[26,27]. If we continue deposition after the interior of the carbon tubule is fully filled with Li, at some point the Li will appear outside the carbon tubule. As shown in Fig. 3b–f and Supplementary Video 9 using dark-field imaging, we observed that after plating through the nanopores, Li first produces a complete wetting, rapidly spreading along the outer surface with zero contact angle up to a distance of 140 nm, before finally pushing downward[28]. This suggests that the ZnO_x/Li_2O layer on the MIEC surface helps to induce a strong lithiophilicity.

Finally, to demonstrate a centimetre-scale all-solid-state full-cell battery, we constructed an MIEC tubular matrix using about 10^{10} cylinders, each with an aspect ratio of several hundred, capped by solid electrolyte (Fig. 4). The counter-electrode is $LiFePO_4$. To fabricate the tubular MIEC matrix, we first used chemical vapour deposition (CVD) to grow a layer of carbon on the inner surface of free-standing anodic aluminium oxide (AAO) that acted as a template. Next, a layer of Pt was deposited on the bottom of the AAO by sputtering, to act as the current

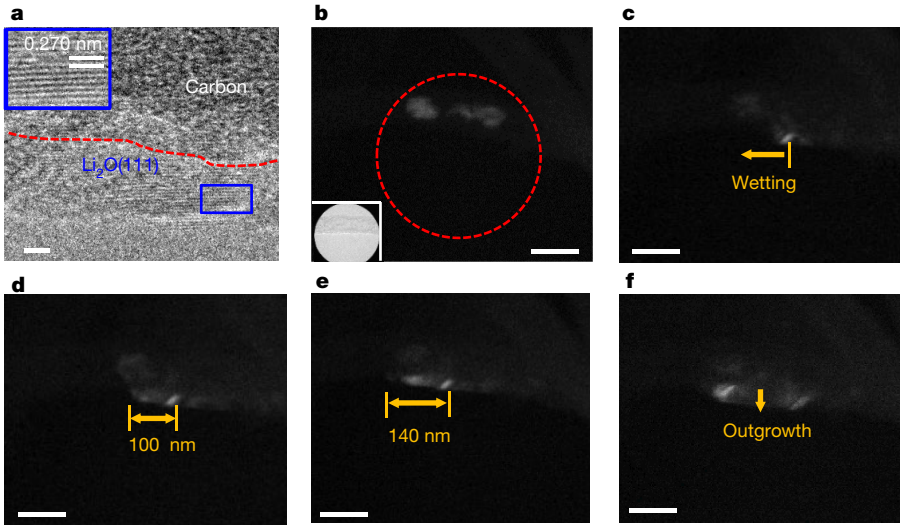

Fig. 3 | Lithiophilicity from ZnO_x. a, HRTEM image of a layer of Li_2O on the outer surface of a carbon tubule. The inset expands the blue-box region, where lattice fringes of Li_2O (111) are seen. **b**–**f**, Snapshots of dark-field imaging of Li_{bcc} wetting the tubule outer surface as a function of time, with **b** showing the Li_{bcc} already plated inside the carbon tubule, **c** to **e** showing facile wetting on the outside the with spreading distance labelled by yellow arrows, and **f** showing final pushing downward ('Outgrowth'). For the dark-field imaging, the $(\bar{1}\bar{1}0)$ diffraction beam of the Li crystal shown in **b** is allowed to pass through the objective aperture, and the red dashed circle denotes the selected-area aperture also shown in the inset of **b**. See Supplementary Video 9. Scale bars: **a**, 2 nm; **b**–**f**, 100 nm.

collector and mechanical support. Then, the AAO was etched away to yield the carbonaceous MIEC tubular matrix[29], as shown in Fig. 4a–d. To enhance the lithiophilicity of the carbonaceous MIEC tubular matrix, a 1-nm-thick ZnO layer was deposited onto the surface of the carbon cylinders by atomic layer deposition (Supplementary Fig. 19). This construction, several centimetres in extent and 50 μm thick, sits on the Pt current collector (Supplementary Fig. 20). Indentation tests[30] show a hardness of about 65 MPa (Supplementary Fig. 21), which is higher than the internal pressurization limit (see Methods section 'Quantitative analysis'). We then cap the MIEC tubular matrix by a film of PEO-based/LiTFSI solid electrolyte, 50 μm thick. A layer of LiPON about 200 nm thick was pre-deposited into the carbon tubules by sputtering to obstruct the open pores (Supplementary Fig. 22). LiPON has a much poorer ionic conductivity than PEO-based/LiTFSI solid electrolyte, and approximates as the electron- and Li-ion insulator (ELI) roots shown in yellow in Fig. 1 that affix MIECs to the solid electrolyte. It also prevents inflow of the polymeric solid electrolyte into the MIEC tubules during testing at 55 °C. The cathode was constructed from the active material $LiFePO_4$ (60 wt%), polyethylene oxide (PEO, 20 wt%), LiTFSI (10 wt%) and carbon black (10 wt%). The mass loading is 4–6 mg $LiFePO_4$ per cm^2 in full cells. In half cells, we use a superabundant Li metal chip (more than 100× excess) as the opposite electrode. No (ionic) liquid or gel electrolyte of any kind was used in our centimetre-scale battery experiments. For making the full cell with a small lithium inventory compared to the cathode capacity, we first pre-deposited 1× excess Li into the MIEC tubules electrochemically from the half cell.

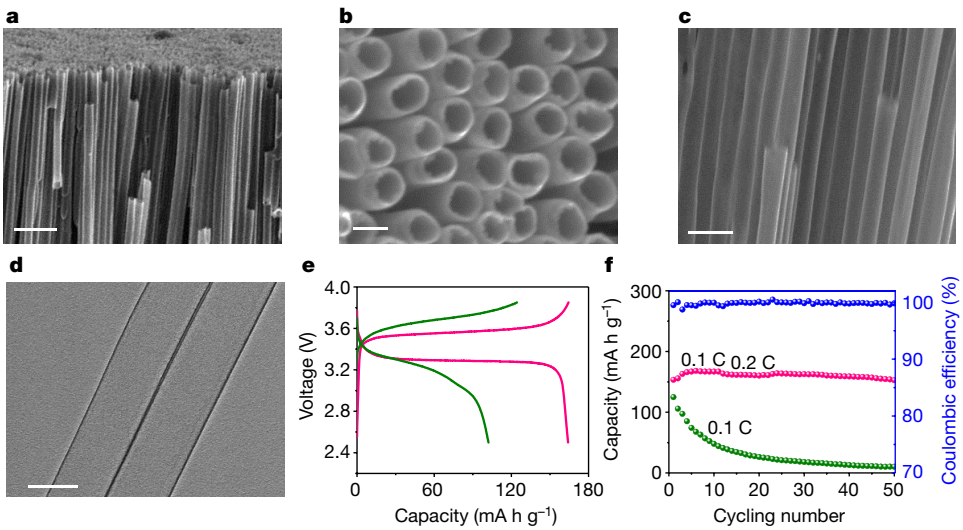

Fig. 4 | Electrochemical performance of scaled-up Li metal cell with about 10^{10} MIEC cylinders. a–**d**, Field emission SEM (FESEM; **a**–**c**) and TEM (**d**) images of the carbonaceous MIEC tubules. **e**, **f**, Charge/discharge profiles at 0.1 C (**e**) and cycling life (**f**) of the all-solid-state (1× excess) Li_{bcc}-pre-deposited MIEC/SE/$LiFePO_4$ batteries. The magenta (capacity) and blue (coulombic efficiency) colours indicate the use of 3D MIEC tubules on Pt foil as a Li host, the discharge capacity of which reaches 164 mA h g^{-1} at 0.1 C and 157 mA h g^{-1} at 0.2 C, while the green colour indicates the use of 2D carbon-coated Cu foil as a Li host. Scale bars: **a**, 1 μm; **c**, 500 nm; and **b**, **d**, 200 nm.

In half-cell tests, we could cycle a large amount of Li with a substantial areal capacity up to 1.5 mA h cm^{-2}. Compared with the control experiment using carbon-coated Cu foil as the Li host, the half cell with the 3D MIEC tubular matrix shows a lower overpotential (39 mV versus 250 mV at 0.125 mA cm^{-2}) and a much higher coulombic efficiency (97.12% versus 74.34% at 0.125 mA cm^{-2}), as well as much better cycling stability (Supplementary Figs. 23, 24). More importantly, in full-cell tests, with only 1× excess Li pre-deposited inside the MIEC tubules, the all-solid-state full cell shows a lower overpotential (0.25 V versus 0.45 V), a higher discharge capacity (164 mA h g^{-1} versus 123 mA h g^{-1}) and a much higher coulombic efficiency (99.83% versus 82.22%) at 0.1 C (Fig. 4e). This full cell shows almost no degradation for more than 50 cycles (Fig. 4f), and the gravimetric capacity of our Li/MIEC composite anode reaches a remarkable value of about 900 mA h g^{-1}. This validates the MIEC architecture for an all-solid-state alkali metal battery, which has been taken from mechanistic concepts to quantitative theory and design to the realm of practice.

Online content

Any methods, additional references, Nature Research reporting summaries, source data, extended data, supplementary information, acknowledgements, peer review information; details of author contributions and competing interests; and statements of data and code availability are available at https://doi.org/10.1038/s41586-020-1972-y.

1. Porz, L. et al. Mechanism of lithium metal penetration through inorganic solid electrolytes. *Adv. Energy Mater*. **7**, 1701003 (2017).
2. Armstrong, R. D., Dickinson, T. & Turner, J. The breakdown of β-alumina ceramic electrolyte. *Electrochim. Acta* **19**, 187–192 (1974).
3. Yang, C. et al. Continuous plating/stripping behavior of solid-state lithium metal anode in a 3D ion-conductive framework. *Proc. Natl Acad. Sci. USA* **115**, 3770–3775 (2018).
4. Liu, Y. et al. Transforming from planar to three-dimensional lithium with flowable interphase for solid lithium metal batteries. *Sci. Adv*. **3**, eaao0713 (2017).
5. Monroe, C. & Newman, J. The impact of elastic deformation on deposition kinetics at lithium/polymer interfaces. *J. Electrochem. Soc*. **152**, A396–A404 (2005).
6. Suo, L. et al. Fluorine-donating electrolytes enable highly reversible 5-V-class Li metal batteries. *Proc. Natl Acad. Sci. USA* **115**, 1156–1161 (2018).
7. Li, Y. et al. Atomic structure of sensitive battery materials and interfaces revealed by cryo-electron microscopy. *Science* **358**, 506–510 (2017).
8. Lu, J., Chen, Z., Pan, F., Cui, Y. & Amine, K. High-performance anode materials for rechargeable lithium-ion batteries. *Electrochem. Energy Rev*. **1**, 35–53 (2018).
9. Devaux, D. et al. Failure mode of lithium metal batteries with a block copolymer electrolyte analyzed by X-ray microtomography. *J. Electrochem. Soc*. **162**, A1301–A1309 (2015).
10. Harry, K. J., Hallinan, D. T., Parkinson, D. Y., MacDowell, A. A. & Balsara, N. P. Detection of subsurface structures underneath dendrites formed on cycled lithium metal electrodes. *Nat. Mater*. **13**, 69 (2014).
11. Maslyn, J. A. et al. Growth of lithium dendrites and globules through a solid block copolymer electrolyte as a function of current density. *J. Phys. Chem. C* **122**, 26797–26804 (2018).
12. Harry, K. J., Liao, X., Parkinson, D. Y., Minor, A. M. & Balsara, N. P. Electrochemical deposition and stripping behavior of lithium metal across a rigid block copolymer electrolyte membrane. *J. Electrochem. Soc*. **162**, A2699–A2706 (2015).
13. Richards, W. D., Miara, L. J., Wang, Y., Kim, J. C. & Ceder, G. Interface stability in solid-state batteries. *Chem. Mater*. **28**, 266–273 (2016).
14. Kim, S. et al. Electrochemically driven mechanical energy harvesting. *Nat. Commun*. **7**, 10146 (2016).
15. Jin, C. et al. 3D lithium metal embedded within lithiophilic porous matrix for stable lithium metal batteries. *Nano Energy* **37**, 177–186 (2017).
16. Zhao, J. et al. Air-stable and freestanding lithium alloy/graphene foil as an alternative to lithium metal anodes. *Nat. Nanotechnol*. **12**, 993–999 (2017).
17. Yan, K. et al. Selective deposition and stable encapsulation of lithium through heterogeneous seed growth. *Nat. Energy* **1**, 16010 (2016).
18. Frost, H. & Ashby, M. *Deformation-Mechanism Maps* (Pergamon, 1982).
19. Zhu, T. & Li, J. Ultra-strength materials. *Prog. Mater. Sci*. **55**, 710–757 (2010).
20. Nitta, N. & Yushin, G. High-capacity anode materials for lithium-ion batteries: choice of elements and structures for active particles. *Part. Part. Syst. Charact*. **31**, 317–336 (2014).
21. Chen, Y. et al. Nitrogen-doped carbon for sodium-ion battery anode by self-etching and graphitization of bimetallic MOF-based composite. *Chem* **3**, 152–163 (2017).
22. Zheng, H., Liu, Y., Mao, S. X., Wang, J. & Huang, J. Y. Beam-assisted large elongation of in situ formed Li_2O nanowires. *Sci. Rep*. **2**, 542 (2012).
23. Liu, Y. et al. Lithium-coated polymeric matrix as a minimum volume-change and dendrite-free lithium metal anode. *Nat. Commun*. **7**, 10992 (2016).
24. Li, S. et al. Developing high-performance lithium metal anode in liquid electrolytes: challenges and progress. *Adv. Mater*. **30**, 1706375 (2018).
25. Zhang, Y. et al. High-capacity, low-tortuosity, and channel-guided lithium metal anode. *Proc. Natl Acad. Sci. USA* **114**, 3584–3589 (2017).
26. Sun, J. et al. Liquid-like pseudoelasticity of sub-10-nm crystalline silver particles. *Nat. Mater*. **13**, 1007–1012 (2014).
27. Yang, Y., Kushima, A., Han, W., Xin, H. & Li, J. Liquid-like, self-healing aluminum oxide during deformation at room temperature. *Nano Lett*. **18**, 2492–2497 (2018).
28. Kushima, A. et al. Liquid cell transmission electron microscopy observation of lithium metal growth and dissolution: root growth, dead lithium and lithium flotsams. *Nano Energy* **32**, 271–279 (2017).
29. Moon, S. et al. Encapsulated monoclinic sulfur for stable cycling of Li-S rechargeable batteries. *Adv. Mater*. **25**, 6547–6553 (2013).
30. Cao, G. & Gao, H. Mechanical properties characterization of two-dimensional materials via nanoindentation experiments. *Prog. Mater. Sci*. **103**, 558–595 (2019).

Methods

Synthesis of carbon hollow tubules

The synthesis of the carbon tubules was similar to that used in our previous work[21]. 1 g of polyacrylonitrile (PAN, Aldrich) and 1.89 g of $Zn(Ac)_2{\cdot}2H_2O$ were dissolved in 30 ml of dimethylformamide (DMF, Aldrich) solvent to obtain the electrospinning solution. A working voltage of 17 kV, a flow rate of 0.05 mm min^{-1}, and an electrospinning distance of 20 cm were used to synthesize the PAN/$Zn(Ac)_2$ composite fibres. A layer of zeolitic imidazolate framework (ZIF-8) can be formed on the surface of the composite fibres by adding them to an ethanol solution of 2-methylimidazole (0.65 g, Aldrich). The introduction of a trace amount of cobalt acetate into the composite fibres can promote the graphitization of the carbon tubules. The synthesized core-shell composite fibres were heated at 600–700 °C for 12 h to obtain the hollow carbon tubules with some ZnO_x.

In situ transmission electron microscopy

This was conducted using a JEOL 2010F TEM at 200 kV with a Nanofactory STM/TEM holder[31]. The solid-state nanobattery contains Li metal, solid electrolyte and the prepared carbon tubules with ZnO_x. The Li metal was applied to a tungsten probe in a glove box filled with Ar gas, and the prepared carbon tubules were adhered to half a TEM copper grid by silver conductive epoxy. For a typical example of a soft solid electrolyte, sufficient poly(ethylene oxide) (PEO) and lithium bis(trifluoromethanesulfonyl)imide (LiTFSI) were dissolved in 1-butyl-1-methylpyrrolidinium bis(trifluoromethylsulfonyl)imide (ionic liquid). The Li metal on the tungsten probe was capped by the obtained solid electrolyte with a thickness of ~50 μm inside the glove box filled with Ar gas. After loading the battery components into the TEM, the end with solid electrolyte covering the Li metal on the tungsten probe was manipulated to get a contact with the carbon tubules on the TEM copper grid to complete the assembly of a nanobattery. Lithium plating and stripping in the carbon tubules were realized by applying −2 V and +2 V with respect to the lithium metal.

Electron radiation damage control

In the in situ TEM experiments, we reduced electron beam damage as much as possible. Li metal is sensitive to electron beam irradiation in the TEM, owing to elastic and inelastic scattering[32]. The elastic (electron–nucleus) scattering can lead to sputtering damage, and the inelastic (electron–electron) scattering can cause damage by specimen heating and radiolysis[7,33].

In our low-magnification TEM images and videos showing Li plating and stripping inside the tubule, a low electron beam current of around 1.5 mA cm^{-2} was used to minimize beam damage. The images were taken at a slightly underfocused condition to enhance the contrast. We blanked the beam before recording the video, and limited experiment recording time to less than 2 min. The beam was blanked for most of the time while plating and stripping Li, except for some necessary observations. For taking the SAED patterns of Li plated inside the tubule, a broad electron beam with a low electron beam current of 1 mA cm^{-2} was used. We took the patterns as quickly as possible to lower the amount of irradiation damage. For taking the HRTEM image of Li plated inside the tubule, an electron beam current of around 0.3 A cm^{-2} was used. The HRTEM image captured the fresh Li crystal when it first appeared inside the camera field, showing the lattice fringes of $(110)_{bcc}$ planes. The Li lattice fringes remained for several seconds before vanishing owing to electron beam irradiation damage.

The carbon tubules help to reduce irradiation damage when imaging Li_{bcc} inside the tubules (Supplementary Figs. 25–27). As the Li_{bcc} is inside the wall of the tubule, this helps to reduce the sputtering loss. In the case of inelastic scattering, the tubule may also act as a thermal/electron conductor covering the lithium metal, helping to release some heat by electron irradiation. Furthermore, the electrochemical plating can continually replenish fresh Li_{bcc} in the region under irradiation, which may also help the HRTEM imaging.

We have also carried out in situ TEM experiments with the electron beam blanked. We first set up the nanobattery inside the TEM, placing the selected-area aperture on the still-hollow carbon tubule, and turned on the SAED mode in advance. During these steps, we did not apply any bias potential (the bias potential is required to deposit Li metal inside the carbon tubule). After this preparation, we turned off the electron beam ('blind' condition). With no electron beam present, we applied bias potential for some time to deposit Li metal inside the tubule. We then turned on the electron beam (at a low current density of 1 mA cm^{-2}), and immediately the sharp SAED pattern appeared on the TEM CCD window. The single crystal feature was later identified as the Li_{bcc} phase from its measured lattice constant (Supplementary Fig. 28).

Electron energy-loss spectroscopy (EELS)

The EELS spectra were taken in the STEM mode with a spot size of 1 nm, with a semi-convergence angle of about 5 mrad and a semi-collection angle of about 10 mrad. For the thickness calculation in Supplementary Fig. 8, the absolute log-ratio method was used[34], where $\frac{t}{\lambda} = \ln\left(\frac{I_t}{I_0}\right)$ (t stands for thickness, λ stands for effective mean free path, I_t is the intensity integration under the whole EELS spectrum, and I_0 is the intensity integration under the zero loss peak). In addition to the accelerating voltage, semi-convergence and semi-collection angles, to calculate λ the effective atomic number Z_{eff} was also needed. We estimate $Z_{eff} = 6$ for the carbon tubule before Li plating. After Li plating, both Li and the wall of the carbon tubule existed at the location where we recorded the EELS signal. In this case, we can estimate the rough atomic ratio between Li and C to be 0.56:1 when considering the observed geometry of the tubule, with an inner diameter of ~100 nm and a wall thickness of ~28 nm. Using the formula

$$Z_{\text{eff}} = \frac{\sum_i f_i Z_i^{1.3}}{\sum_i f_i Z_i^{0.3}}$$

we obtain $Z_{eff} = 5.1$ (after Li plating).

The thicknesses before and after Li plating were thus calculated to be ~68 nm and ~160 nm respectively from the EELS spectra recorded in Supplementary Fig. 8, and the thickness difference (corresponding to the thickness of Li plated) was estimated to be ~92 nm. The background contribution under the edge can be estimated from the pre-edge area, and the K-edge of Li was obtained by background subtraction.

Other characterizations

The synthesized materials were characterized by TEM, high-resolution TEM (HRTEM), field emission scanning electron microscopy (FESEM, FEI Helios 600 Dual Beam FIB), energy-dispersive X-ray spectroscopy (EDX, Oxford) and X-ray photoelectron spectroscopy (XPS, PHI5600).

Synthesis of MIEC 3D electrode

First, the chemical vapour deposition (CVD) method was applied, using 90 sccm C_2H_2 at 640 °C, which grows a layer of carbon onto the inner surface of anodic aluminium oxide (AAO) that acted as the template. Next, a layer of Pt was deposited by sputtering on the bottom of the AAO; it acted as the current conductor and as mechanical support. Then, the AAO was etched to yield the carbonaceous MIEC tubular matrix by employing a 3 M NaOH aqueous solution with a small amount of ethanol added. To enhance the lithiophilicity of the MIEC tubules, a 1-nm-thick ZnO layer was deposited onto the inner surfaces of the MIEC tubular matrix by ALD (atomic layer deposition).

Li/solid electrolyte/MIEC half cell

To avoid the inflow of polymeric solid electrolyte into the MIEC tubules during testing at 55 °C, a layer of LiPON ~200 nm thick was deposited onto the MIEC tubules by sputtering to obstruct the open pores. A

PEO-based/LiTFSI film was used as a typical solid electrolyte (from KISCO Ltd). The 2032 coin cells were prepared by pressing the MIEC tubular matrix onto one side of the solid electrolyte film and a Li metal chip onto the other side. The obtained Li/solid electrolyte/MIEC tubular matrix half cell was tested at current densities of 0.125, 0.25 and 0.5 mA cm^{-2}. The half cells were cycled a few times to stabilize the interface between solid electrolyte and electrode. The Coulombic efficiency was obtained from the ratio of discharge and charge capacity. For comparison, 2D carbon-coated Cu foil was used to prepare a Li/solid electrolyte/carbon-coated Cu foil cell.

All-solid-state full cell

The $LiFePO_4$ cathode was constructed from $LiFePO_4$ powder (the active material, 60 wt%), polyethylene oxide (PEO, 20 wt%), LiTFSI (10 wt%), and carbon black (10 wt%). The mass loading is 4–6 mg $LiFePO_4$ per cm^2. We predeposited 1× excess Li into the MIEC tubules from the half cell. The 2032 coin cells were prepared with Li-deposited MIEC tubules as the anode, the $LiFePO_4$ electrode as the cathode and solid electrolyte in an Ar-filled glove box. The all-solid-state battery was tested at 55 °C with a LAND battery tester between 2.5 V and 3.85 V. We also predeposited 1× excess Li onto the carbon-coated Cu foil of the control battery before the full cell testing.

Quantitative analysis

Internal gas pressure accommodation. For mechanical stability, it is in practice difficult to construct a vacuum-filled tubular matrix, so we will assume that initially we have an inert gas phase in the white region in Fig. 1 with P_{gas} = 1 atm. The gas-tightness of the solid electrolyte layer must be guaranteed, because otherwise Li metal will easily plate or flow through the solid electrolyte, shorting to the cathode. Thus, when Li metal is deposited inside a tubule, the gas phase must be compressed. If the current collector (say Cu) and the MIEC walls are also hermetically sealed, then local P_{gas} will increase as more and more Li metal is deposited inside, up to possibly tens of atmospheres (a few MPa) if the compression ratio is something like 10×. The creeping Li metal can act as a piston, as we have seen from the Nernst equation that $P_{LiMetal}$ can[1] easily reach hundreds of MPa. However, owing to unavoidable heterogeneities, the amount of Li metal deposited may not be the same between adjacent cylinders, and this will cause a pressure difference, ΔP_{gas}, between adjacent cylinders that can bend the MIEC wall. If the MIEC wall (red region in Fig. 1) is not mechanically ductile enough, then at a certain point a cell may burst. For this reason, it is better for the MIEC wall to be permeable, so P_{gas} can then equilibrate from cell to cell. Then the internal pressure will be more homogenously distributed, ensuring that the left chamber in Fig. 1 will not expand and crush the right chamber by bending the wall.

Geometric design. While the in situ TEM experiments give us confidence that MIEC electrochemical cells work at the 'single cylinder' or 'few-cylinders' level, transport and mechanical durability issues will determine how well the cell will work in practice at cm × cm scale, with a massive number (~10^{10}) of parallel cylinders. The typical areal capacity Q and current density $J \equiv dQ/dt$ demanded by industrial applications are of the order 3 mA h cm^{-2} and 3 mA cm^{-2}, respectively. Typical overpotentials U of lithium-metal-containing anodes (versus Li^+/Li) are of the order of 50 mV. With unavoidable heterogeneities among the ~10^{10} cylinders, transport/reaction limitations may vary from location to location. With $P_{LiMetal}$ in MPa and U in V, we have $\max P_{LiMetal} = 7{,}410U$, so for U = 50 mV, $\max P_{LiMetal}$ = 370 MPa: the higher the overpotential, the larger $\max P_{LiMetal}$, and the more severe the local mechanical degradations can be. We cannot allow the overpotential U, a global quantity, to rise too high; but U is still responsible for driving a global average current density J. This means the average transport conductance should be better than ~3 mA cm^{-2} / 50 mV = 0.06 S cm^{-2} as an order-of-magnitude estimate, otherwise the requisite pressure might be too high and the MIEC tubules may burst somewhere. The effective transport conductance of the tubular matrix is $(\kappa_{MIEC}/h) \times w/(w+W)$, where κ_{MIEC} (in S cm^{-1}) is an effective Li conductivity, and $w/(w+W)$ is the fill factor by MIEC (assuming straight pores and tortuosity = 1). In order to get $Q \approx 3$ mA h cm^{-2}, h needs to be at least ~20 μm, taking into account the inert host volume (see Supplementary Fig. 29 for calculated capacity with the tubular matrix geometry). So we get an effective longitudinal transport requirement:

$$\kappa_{MIEC} \times w/(w+W) > 0.06\ \text{S cm}^{-2} \times 20\ \mu\text{m} = 0.12\ \text{mS cm}^{-1} \quad (1)$$

For MIEC, we have bulk contribution

$$\kappa_{MIEC}^{bulk} \approx e^2 c_{Li} D_{Li}^{bulk}/k_B T \quad (2)$$

where c_{Li} (in cm^{-3}) is the Li atom concentration, and D_{Li}^{bulk} is the tracer diffusivity of Li atoms in bulk MIEC. We should recognize, however, that interfacial diffusion might be significant or even dominant with 100-nm-sized MIEC cylinders, as there can be fast diffusion paths of width $\delta_{interface}$ (typically taken to be 2 Å) at the MIEC/Li_{bcc} incoherent phase boundary (red/grey interface in Fig. 1) or surface (red/white interface in Fig. 1), in which case we need to correct κ_{MIEC} by the following size-dependent factor:

$$\kappa_{MIEC} = \kappa_{MIEC}^{bulk} \times (1 + 2D_{Li}^{interface}\delta_{interface}/D_{Li}^{bulk}w) \quad (3)$$

With bulk diffusivity data culled from table 2 of ref. [20], we see that among the three canonical MIECs—LiC_6 ($c_{Li} = 1.65 \times 10^{22}$ cm^{-3}, optimistic $D_{Li}^{bulk} \approx 10^{-7}$ cm^2 s^{-1}), $Li_{22}Si_5$ ($c_{Li} = 5.3 \times 10^{22}$ cm^{-3}, optimistic $D_{Li}^{bulk} \approx 10^{-11}$ cm^2 s^{-1}) and Li_9Al_4 ($c_{Li} = 4 \times 10^{22}$ cm^{-3}, optimistic $D_{Li}^{bulk} \approx 10^{-9}$ cm^2 s^{-1})—it looks likely that LiC_6 has the largest $c_{Li}D_{Li}^{bulk}$. Putting the values into equation (2), $\kappa_{MIEC}^{bulk}(LiC_6) \approx 0.01$ S cm^{-1}. However, there is large uncertainty in the diffusivity data, so a more conservative estimate might be $D_{Li}^{bulk}(LiC_6) \approx 10^{-8}$ cm^2 s^{-1}, $\kappa_{MIEC}^{bulk}(LiC_6) \approx 1$ mS cm^{-1}. Thus, the minimum MIEC fill factor for LiC_6 is

$$w_{min}/(w_{min}+W) = \frac{0.12\ \text{mS cm}^{-1}}{\kappa_{MIEC}} \approx 0.1$$

and so if $W \approx 100$ nm, one should have minimally $w = w_{min} \approx 10$ nm. This wall thickness happens to also make sense from a mechanical robustness requirement viewpoint. Coincidentally, this geometry is quite close to that of our carbon tubule experiment. The design above is consistent with the fact that graphite or hard carbon anodes used in lithium-ion batteries (LIB) have a film thickness of the order of 100 μm, and the film is known to be able to support a current density of ~3 mA cm^{-2} with an overpotential of ~50 mV. Indeed, referencing to an industrial LIB graphite anode is apt here, because we know they work near the borderline as an anode in charging: if the current density is significantly higher than ~3 mA cm^{-2}, then the local potential would drop below 0 V versus Li^+/Li, and Li_{bcc} would precipitate out, which is a substantial problem for LIB cycle life and safety with liquid electrolyte. Here, we are proposing to turn the problem on its head. We want the Li metal to 'spill out' of the MIEC, but in a controlled fashion, inside the internal tubular cells within a reserved space capped by ELI and solid electrolyte, without excessive $P_{LiMetal}$ build-up and cracking of the solid electrolyte, and without any fresh SEI production (since the expanding/shrinking parts are in contact with MIEC and will stop at ELI, which are both electrochemically absolutely stable against Li metal, so no side reactions are possible electrochemically). Then we only need to ensure mechanical integrity of this 3D solid structure of open-pore MIECs rooted in solid electrolyte via ELI.

If there were no interfacial diffusion contribution, Li_9Al_4 might be a borderline case, with $\kappa_{MIEC}(Li_9Al_4) \approx 0.25$ mS cm^{-1} from equation (2), thus requiring an excessively large MIEC fill factor of

$$w_{min}/(w_{min}+W)=\frac{0.12\ \mathrm{mS\ cm^{-1}}}{\kappa_{MIEC}}\approx 0.5$$

and requiring $w_{min}\approx W\approx 100$ nm. Such a large fill factor is unlikely to be competitive against a graphite anode. Lastly, the bulk Li diffusivity value ($D_{Li}^{bulk}\approx 10^{-11}$ cm^2 s^{-1}) for $Li_{22}Si_5$ is totally unworkable, because $\kappa_{MIEC}(Li_{22}Si_5)\approx 0.003$ mS cm^{-1}, and we cannot satisfy the transport requirement, equation (1). We conclude therefore that if bulk diffusion alone operates in the MIEC, $D_{Li}^{bulk}\approx 10^{-8}$ cm^2 s^{-1} would be workable, $D_{Li}^{bulk}\approx 10^{-9}$ cm^2 s^{-1} would be difficult, and anything lower would be impossible.

Experimentally, when stripping Li metal (Fig. 2j–l, Supplementary Fig. 17 and Supplementary Video 4), we can sometimes create a void plug that grows between the residual Li metal and the solid electrolyte. Yet this gap does not prevent the Li metal from being further stripped in the experiment, growing the void that separates solid electrolyte from the residual lithium. Li metal must therefore flow out from the MIEC wall/surface. This then excludes dislocation power-law creep as a major kinetic mechanism, since dislocation slip cannot occur in the void, and the residual Li metal shows very little mechanical translation (convection) in our experiments, although slight local sliding cannot be excluded. Based on our in situ TEM observations, therefore, the Li metal must be in the Coble creep regime. However, this does not determine whether the Li is transported along the MIEC interior of width w, or along the MIEC/Li metal interface (Supplementary Fig. 4 case) or over the MIEC surface (Fig. 2j-l case) of width $\delta_{interface}$, and then plated to the tip of the Li metal via Li metal surface diffusion, as illustrated in Fig. 1. A theoretical bound is necessary. According to NMR measurements[35], bulk b.c.c. Li metal has $D_{Li}^{bulk}\approx 4\times 10^{-11}$ cm^2 s^{-1} at room temperature, which we know from the calculations above is two orders of magnitude too sluggish to support the observed Li metal kinetics. For surface diffusivity of Li on b.c.c. Li metal, the empirical formula[36]

$$D_{Li}^{surface}=0.014\exp(-6.54T_M/T)\ \mathrm{cm^2\ s^{-1}} \quad (4)$$

has been verified to work quite well for monatomic metals. For instance, Sn, another low-melting-point metal ($T_M=232$ °C), was found to have surface diffusivity $D_{Sn}^{surface}\approx 1\times 10^{-7}$ cm^2 s^{-1} at room temperature by direct mechanical creep deformation experiments[37], while equation (4) predicts 2×10^{-7} cm^2 s^{-1}. Equation (4) predicts $D_{Li}^{surface}=7\times 10^{-7}$ cm^2 s^{-1} in b.c.c. Li at room temperature. This is 70× larger than that of $D_{Li}^{bulk}\approx 10^{-8}$ cm^2 s^{-1} in LiC_6. The geometry factor $2\delta_{interface}/w$, on the other hand, is of the order of 4 Å/10 nm = 1/25. Thus, if one takes an optimistic estimate that $D_{Li}^{interface}\approx D_{Li}^{surface}$, then the interfacial diffusion contribution can be 3× that of the bulk MIEC diffusional contribution even for LiC_6. The MIEC/Li metal phase boundary has a lower atomic free volume than the free Li metal surface, so we expect $D_{Li}^{interface}$ could be a factor of a few smaller than $D_{Li}^{surface}=7\times 10^{-7}$ cm^2 s. Experimental diffusivity data for metals[38] suggest that $D_{Li}^{interface}\approx 2\times 10^{-7}$ cm^2 s^{-1}. Thus, $D_{Li}^{interface}$ will definitely dominate over bulk MIEC diffusion for Li_9Al_4 and $Li_{22}Si_5$, as the ratio $D_{Li}^{interface}/D_{Li}^{bulk}$ (200 for Li_9Al_4 and 20,000 for $Li_{22}Si_5$) easily overwhelms the geometric factor $2\delta_{interface}/w$ (1/25 for $w=10$ nm). The bulk MIEC contribution can thus be ignored for the electrochemical design, and regardless of MIEC choices we predict an effective $\kappa_{MIEC}\approx 1$ mS cm^{-1}, which would satisfy the longitudinal transport requirement, equation (1), for an MIEC fill factor of $w/(w+W)=0.1$. This predicts that the MIEC tubule concept actually becomes feasible even for Li_9Al_4 and $Li_{22}Si_5$ or any other electrochemically stable MIEC, since diffusion flux along the $\delta_{interface}\approx 2$ Å MIEC/metal incoherent interface or the MIEC surface dominates over the 10 nm MIEC itself. This recognition greatly liberates the MIEC material selection choices, as we can now separate its mechanical function from its ion-transport function. In other words, ion transport along the MIEC is dominated by an 'interfacial MIEC channel' along $\delta_{interface}$, as illustrated in Fig. 1.

Data availability

The datasets generated during and/or analysed during the current study are available from the corresponding author on reasonable request.

31. Yuan, Y., Amine, K., Lu, J. & Shahbazian-Yassar, R. Understanding materials challenges for rechargeable ion batteries with in situ transmission electron microscopy. *Nat. Commun.* **8**, 15806 (2017).
32. Egerton, R. F., Li, P. & Malac, M. Radiation damage in the TEM and SEM. *Micron* **35**, 399–409 (2004).
33. Wang, X. et al. New insights on the structure of electrochemically deposited lithium metal and its solid electrolyte interphases via cryogenic TEM. *Nano Lett.* **17**, 7606–7612 (2017).
34. Malis, T., Cheng, S. C. & Egerton, R. F. EELS log-ratio technique for specimen-thickness measurement in the TEM. *J. Electron Microsc. Tech.* **8**, 193–200 (1988).
35. Mali, M., Roos, J., Sonderegger, M., Brinkmann, D. & Heitjans, P. ^{6}Li and ^{7}Li diffusion coefficients in solid lithium measured by the NMR pulsed field gradient technique. *J. Phys. F* **18**, 403 (1988).
36. Xie, D.-G. et al. In situ study of the initiation of hydrogen bubbles at the aluminium metal/oxide interface. *Nat. Mater.* **14**, 899–903 (2015).
37. Tian, L., Li, J., Sun, J., Ma, E. & Shan, Z-W. Visualizing size-dependent deformation mechanism transition in Sn. *Sci. Rep.* **3**, 2113 (2013).
38. Gjostein, N. A. *Diffusion* (ASM, 1973).

Acknowledgements We acknowledge support by the Department of Energy, Basic Energy Sciences under award number DE-SC0002633 ('Chemomechanics of far-from-equilibrium interfaces'), and by NSF ECCS-1610806. We thank KISCO Ltd for providing the PEO-based/LiTFSI solid electrolyte film.

Author contributions The experiments were conceived and designed by Y.C., Z.W. and J.L.; Y.C. and Z.W. performed the in situ TEM experiments, TEM imaging analysis, materials characterization, and the electrochemical performance assessments; Y.C., Z.W., X.L. and X.Y. synthesized the materials; Y. L., N.W. and J.B.G. helped with the electrochemical characterization; S.Y.K. and Y.-W.M. performed the nanoindentations; Y.C., Z.W. and J.L. wrote the paper; Y.-W.M., Z.W., X.L., X.Y., C.W., W.X., D.Y., F.Y., A.K., G.Z., H.H., J.B.G. and J. L. analysed the data, discussed the results and commented on the manuscript.

Competing interests The authors declare no competing interests.

Additional information
Supplementary information is available for this paper at https://doi.org/10.1038/s41586-020-1972-y.
Correspondence and requests for materials should be addressed to J.L.
Peer review information *Nature* thanks Werner Sitte and the other, anonymous, reviewer(s) for their contribution to the peer review of this work.

nature

https://doi.org/10.1038/s41586-020-1972-y

Supplementary information

Li metal deposition and stripping in a solid-state battery via Coble creep

In the format provided by the authors and unedited

Yuming Chen, Ziqiang Wang, Xiaoyan Li, Xiahui Yao, Chao Wang, Yutao Li, Weijiang Xue, Daiwei Yu, So Yeon Kim, Fei Yang, Akihiro Kushima, Guoge Zhang, Haitao Huang, Nan Wu, Yiu-Wing Mai, John B. Goodenough & Ju Li

Lithium metal deposition and stripping in a solid-state battery via Coble creep

Yuming Chen[1,2‡], Ziqiang Wang[1‡], Xiaoyan Li[1,2,4], Xiahui Yao[1], Chao Wang[1], Yutao Li[5], Weijiang Xue[1], Daiwei Yu[3], So Yeon Kim[1], Fei Yang[1], Akihiro Kushima[6], Guoge Zhang[4], Haitao Huang[4], Nan Wu[5], Yiu-Wing Mai[7], John B. Goodenough[5] & Ju Li[1,*]

[1] Department of Nuclear Science and Engineering and Department of Materials Science and Engineering, Massachusetts Institute of Technology, Cambridge, Massachusetts 02139, USA.

[2] College of Environmental Science and Engineering, Fujian Normal University, Fuzhou 350007, China.

[3] Department of Electrical Engineering and Computer Science, Massachusetts Institute of Technology, Cambridge, Massachusetts 02139, USA.

[4] Department of Applied Physics, Hong Kong Polytechnic University, Hong Kong, China.

[5] Texas Materials Institute and Materials Science and Engineering Program, University of Texas at Austin, Austin, TX 78712, USA.

[6] Advanced Materials Processing and Analysis Center, Department of Materials Science and Engineering, University of Central Florida, Orlando, Florida 32816, USA.

[7] Centre for Advanced Materials Technology (CAMT), School of Aerospace, Mechanical and Mechatronics Engineering J07, The University of Sydney, NSW 2006, Australia.

‡ These authors contributed equally: Y.C. and Z.W.

*Email address: liju@mit.edu (J.L.)

Supplementary Figures

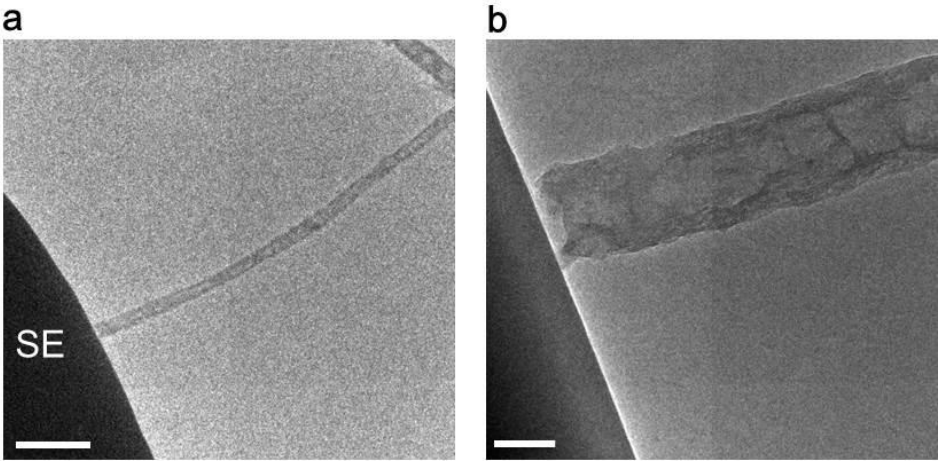

Supplementary Fig. 1 | Contact between the SE and carbon tubule. a, **b**, TEM images of a typical single carbon tubule in contact with SE. Scale bar, **a,** 1μm and **b,** 100 nm.

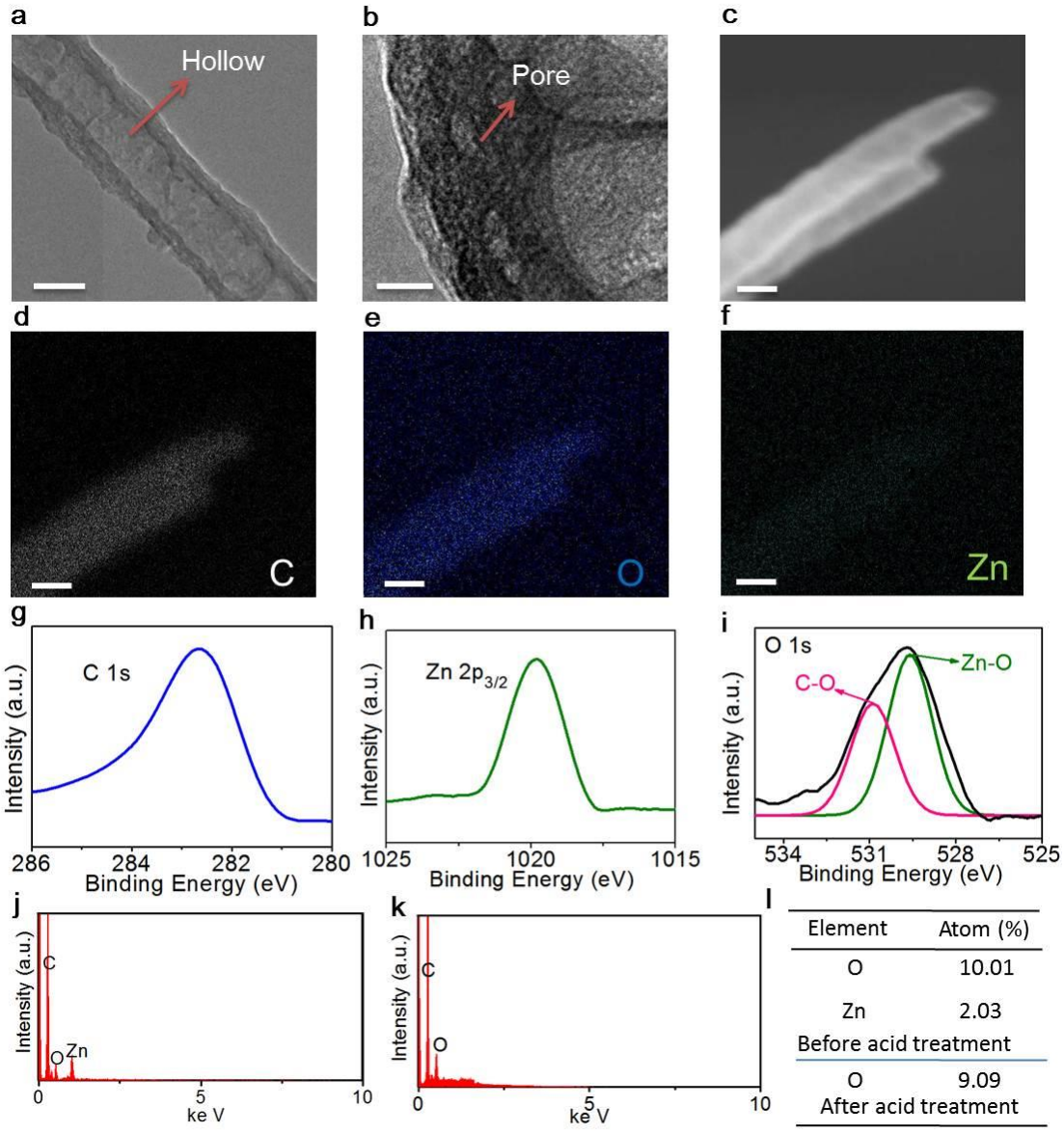

Supplementary Fig. 2 | Characterizations of the carbon tubule with ZnO_x. a, **b**, TEM images of the prepared samples. **c-f**, EDX mapping of the prepared samples. **g-i**, C1s, $Zn2p_{3/2}$ and O1s XPS spectra of the prepared samples. **j**,**k**, EDX spectra of the samples before and after acid treatment. **l**, The ratio of Zn and O in the samples before and after acid treatment. Scale bar, **a, c-f,** 100 nm and **b,** 20 nm.

As shown in Supplementary Fig. 2a,b, the prepared sample shows hollow tubule structure with pores in the wall. The EDX mapping shows a trace of ZnO_x uniformly distributed in the carbon hollow tubules (Supplementary Fig. 2c-f). XPS analysis further confirms the existence of C, Zn and O (Supplementary Fig. 2 g-i). The XPS spectrum of the O1s core can be attributed to a sum of two peaks of C-O and Zn-O (Supplementary Fig. 2i)[1]. x in the ZnO_x can be calculated to be ~ 0.45 based on (10.01-9.09)/2.03 (Supplementary Fig. 2l). The atomic ratio of zinc atoms of zinc oxide to carbon atoms is about 2 %.

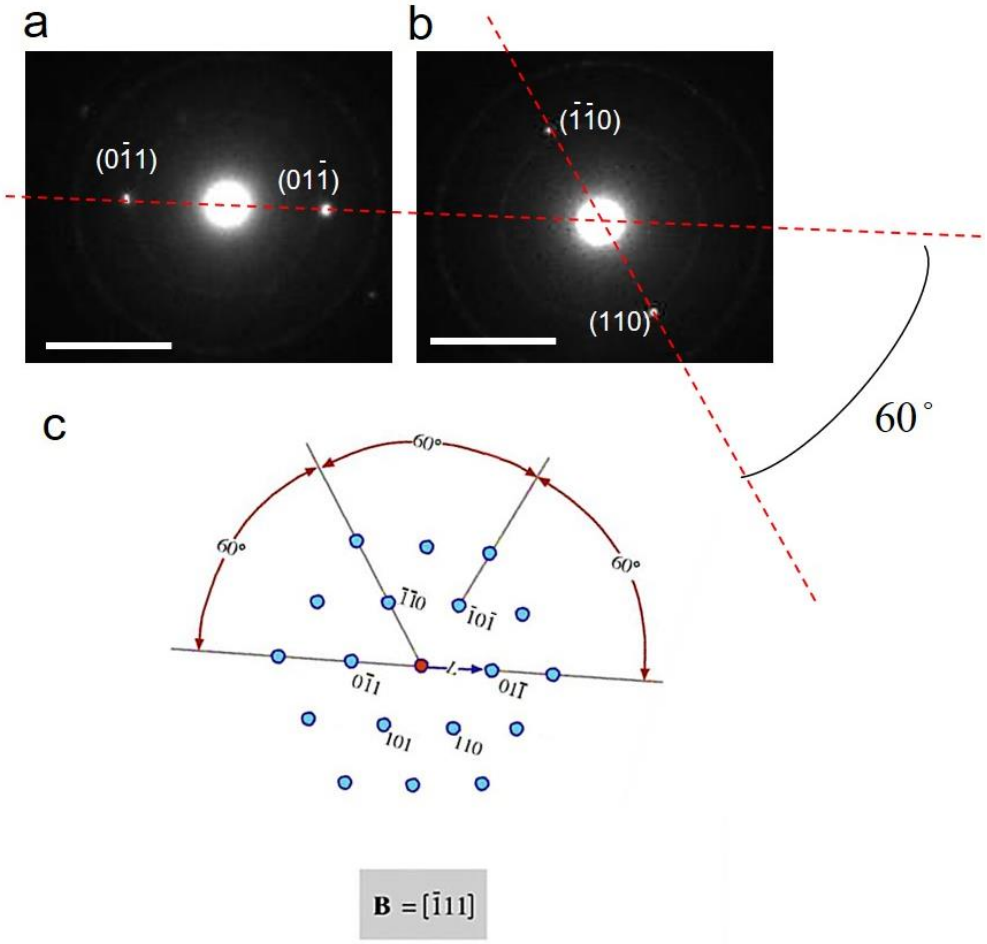

Supplementary Fig. 3 | BCC Li metal crystal phase confirmation. **a**, **b**, SAED patterns taken using a camera length of 100cm (**a**) obtained after Li plating inside carbon tubule with the indexed (1$\bar{1}$0) and (01$\bar{1}$) symmetric diffraction spots for Li_{BCC} and (**b**) then obtained after a rotation of specimen to show the indexed (110) and ($\bar{1}\bar{1}$0) symmetric diffraction spots. **c**, The standard indexed diffraction patterns in [$\bar{1}$11] beam direction under six-fold symmetry of cubic BCC lattice. The two pairs of symmetric diffraction spots in Supplementary Fig. 3a,b present a measured angle of 60° between each other. The indexing and the measured 60° angle between the two pairs of the symmetric spots we obtained are well consistent with the standard diffraction pattern in Supplementary Fig. 3c. Additionally, the distance between the collected diffraction spots also agree with the lattice spacing. Scale bar, 5 nm^{-1}.

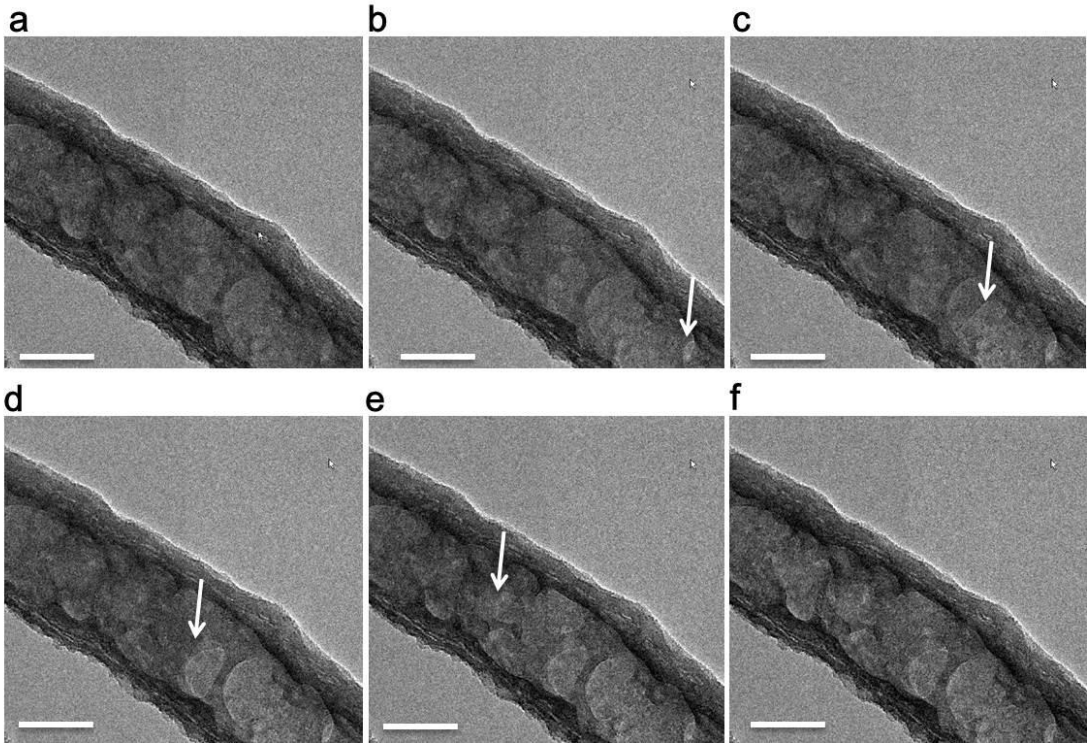

Supplementary Fig. 4 | Li stripping in the carbon tubule. a-f, TEM imaging of Li stripping in a single carbon tubule. Scale bar, 100 nm. The Li inside the hollow tubule can be stripped along the tubule, by retracting the tip.

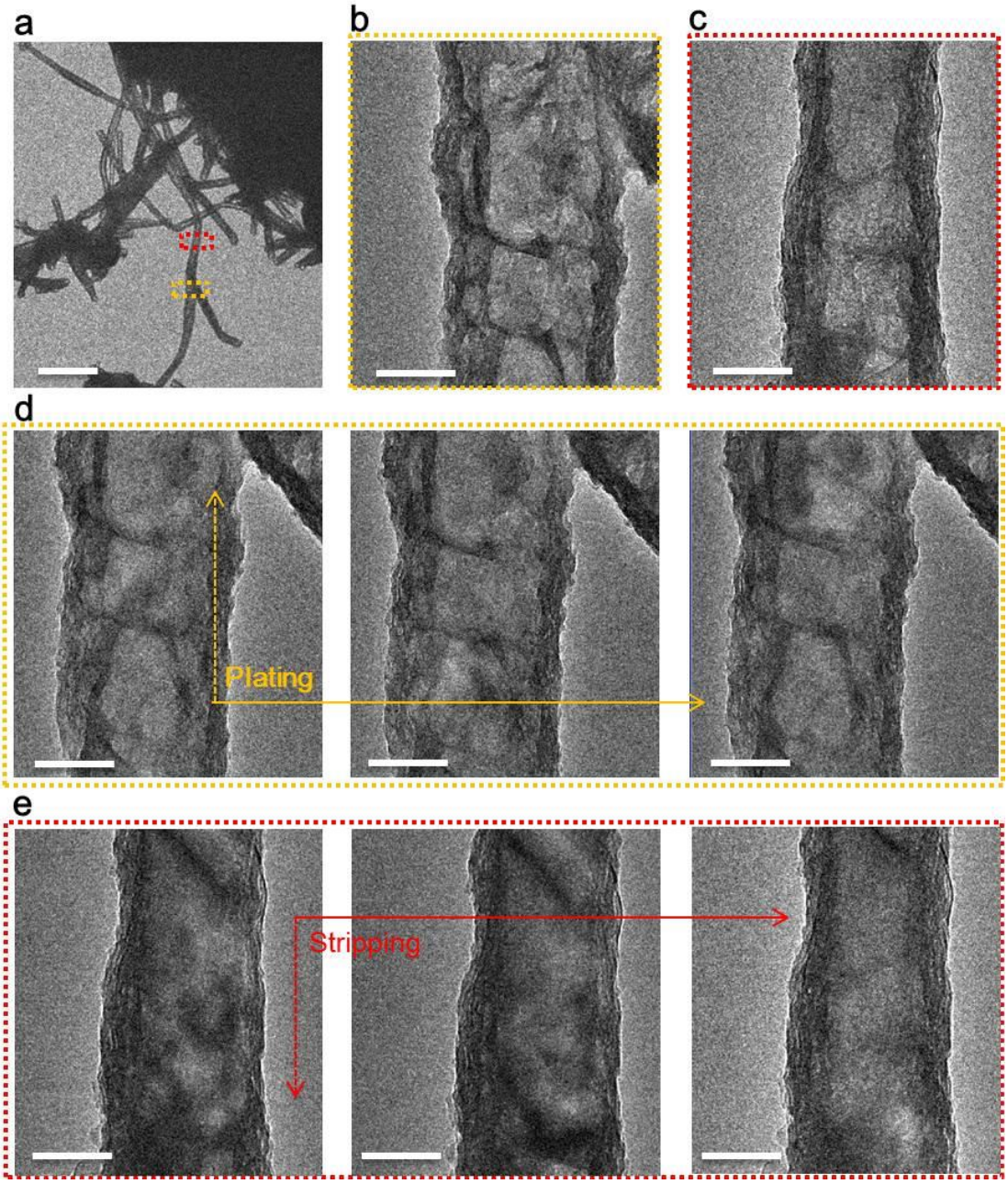

Supplementary Fig. 5 | Li plating/stripping. **a-c,** TEM images of a single long carbon tubule. **d**, **e,** TEM imaging of Li plating (**d**) and Li stripping **(e)** inside the carbon tubule. Scale bar, **a,** 2 μm and **b-e,** 100 nm. We can clearly see Li plating and stripping inside a long and single carbon tubule with the plating process indicated in the yellow dashed frame, and the stripping process indicated in the red dashed frame. The location labeled by the red dashed frame is over 6 μm away from the SE surface, indicating the length of plated Li over 6 μm.

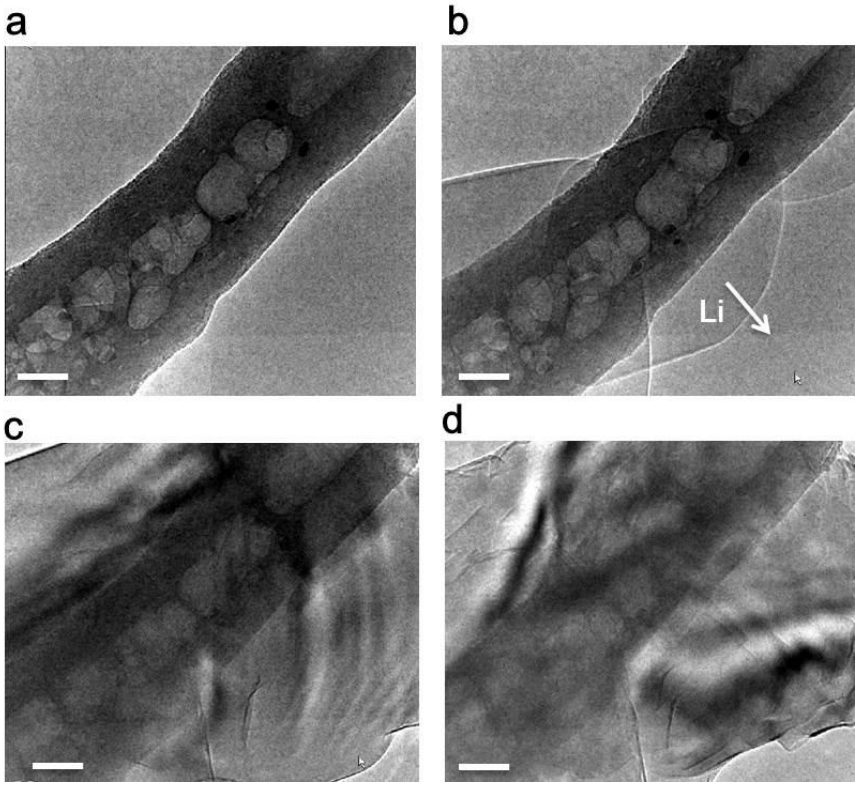

Supplementary Fig. 6 | The overflow of the plated Li out of the tubule under large positive bias. a-d, TEM imaging of the plated Li overflowing from the carbon tubule because of the large bias of 10V applied. Scale bar, 100 nm. When a large bias was applied, a lot of Li can overflow from the tubule, which suggests that Li was fulfilled within the tubule previously.

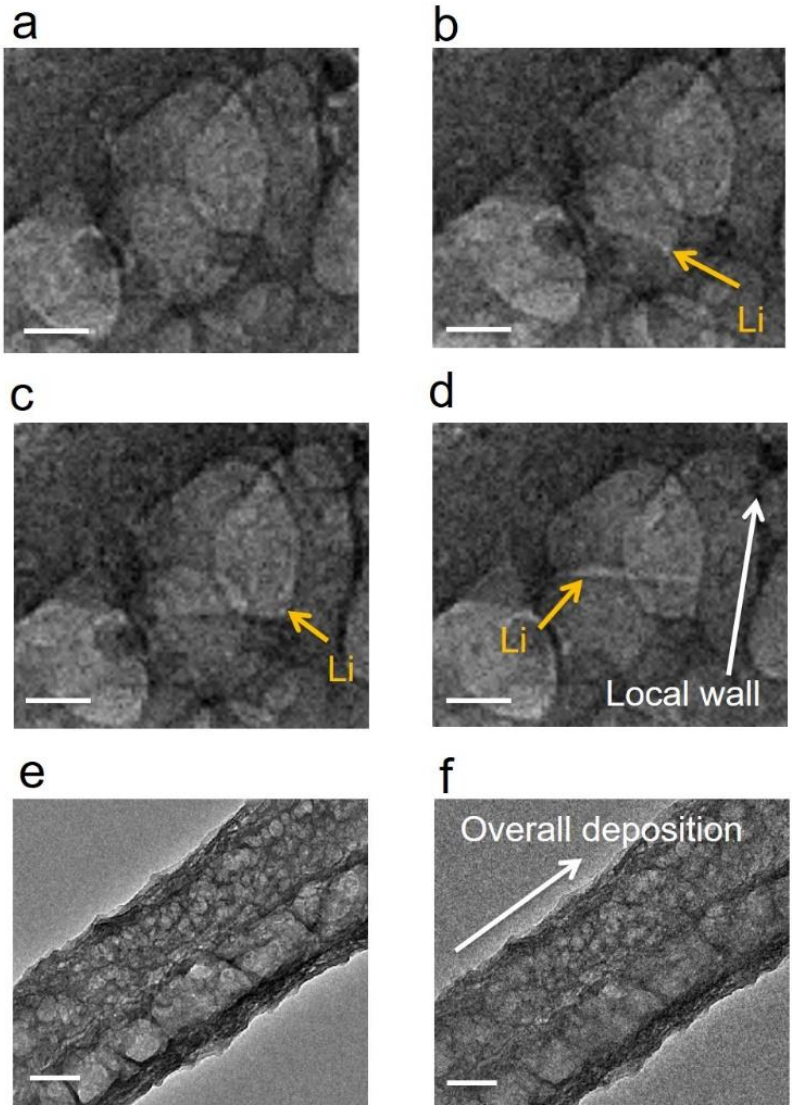

Supplementary Fig. 7 | Li plating/stripping. a-d, TEM imaging of Li_{BCC} plating in 3D porous structures inside the channel. **e**, **f**, TEM images of the channel with 3D obstructions (**e**) before and (**f**) after Li plating. Scale bar, **a-f**, 50 nm and **e**, **f**, 100 nm.

When the channel is filled with 3D obstructions as shown in Supplementary Fig. 7, the mechanism of Li plating/stripping inside these MIEC hosts still follows the interfacial diffusion along the MIEC/Li metal interface, but along a more tortuous path on the local MIEC structures. In a specific area inside the channel, the Li can diffuse along the local 3D MIEC structures inside the channel and then Li plates and fills inside the open pores as shown in the TEM images (Supplementary Fig. 7a-d). However, the thermodynamic driving force by the overpotential (chemical potential) drives an atomic fountain like behavior to fill in the open pores, and on average guides the Li flux along the overall channel direction. The multi-tip-deposition of Li will fill inside the spaces among the 3D MIEC structures. With more and more spaces filled, the overall deposition direction is along the channel (the overall 'rail'). Although the local Li plating may follow 3D structure surface directions, but the overall deposition must be along the channel (Supplementary Fig. 7e,f).

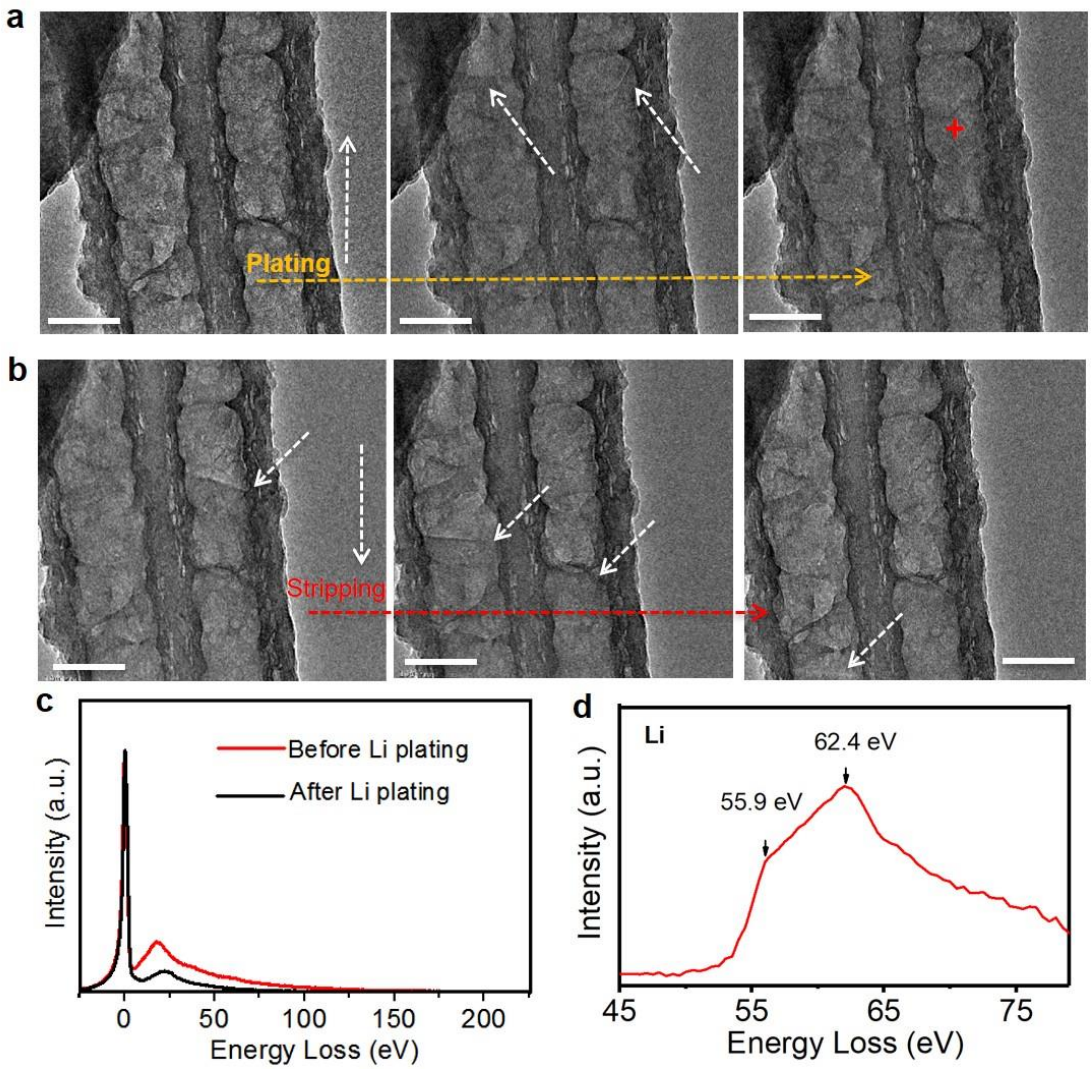

Supplementary Fig. 8 | Li plating/stripping in the double carbon tubules. a, **b**, Li plating and stripping in the double aligned carbon tubules with the plating process (**a**) and the stripping process (**b**) with the fronts indicated by the white arrows, showing that the double hollow tubules can also rail-guide the Li plating/stripping along the tubule. See also Supplementary Video 5. **c**, EELS spectra taken at the position indicated by the red cross in (**a**) before and after Li plating. **d**, The Li K-edge fine structure for EELS after Li plating by background subtraction. Scale bar, 100 nm.

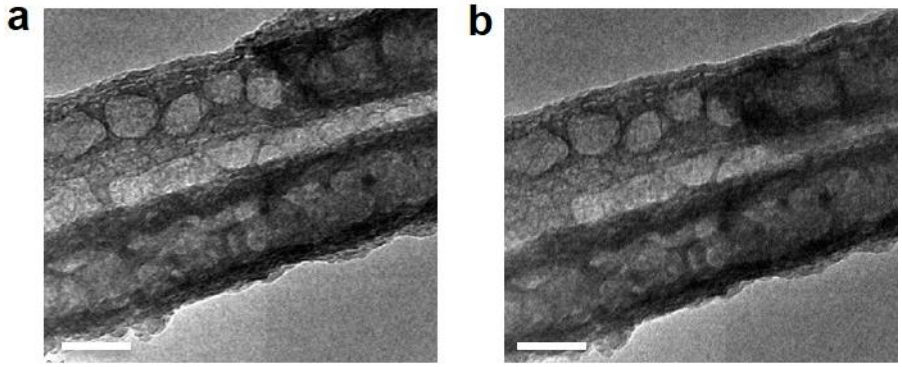

Supplementary Fig. 9 | Li plating in the triple hollow carbons. **a**, **b**, TEM images before (**a**) and after (**b**) Li plating in the triple carbon hollow tubules. Scale bar, 100 nm. The contrast in (**b**) is still darker after Li plating, although it's a little blurring due to the thicker carbon walls.

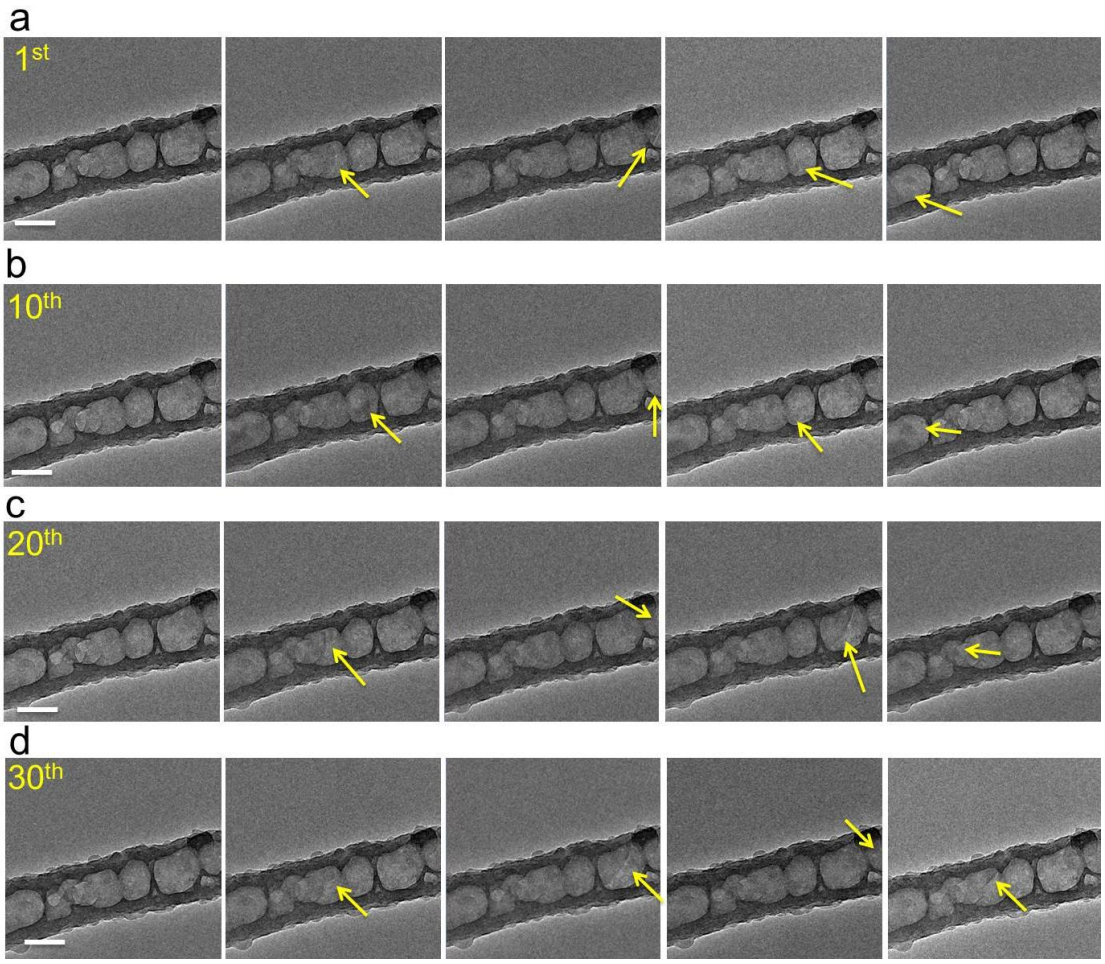
a
1st
b
10th
c
20th
d
30th

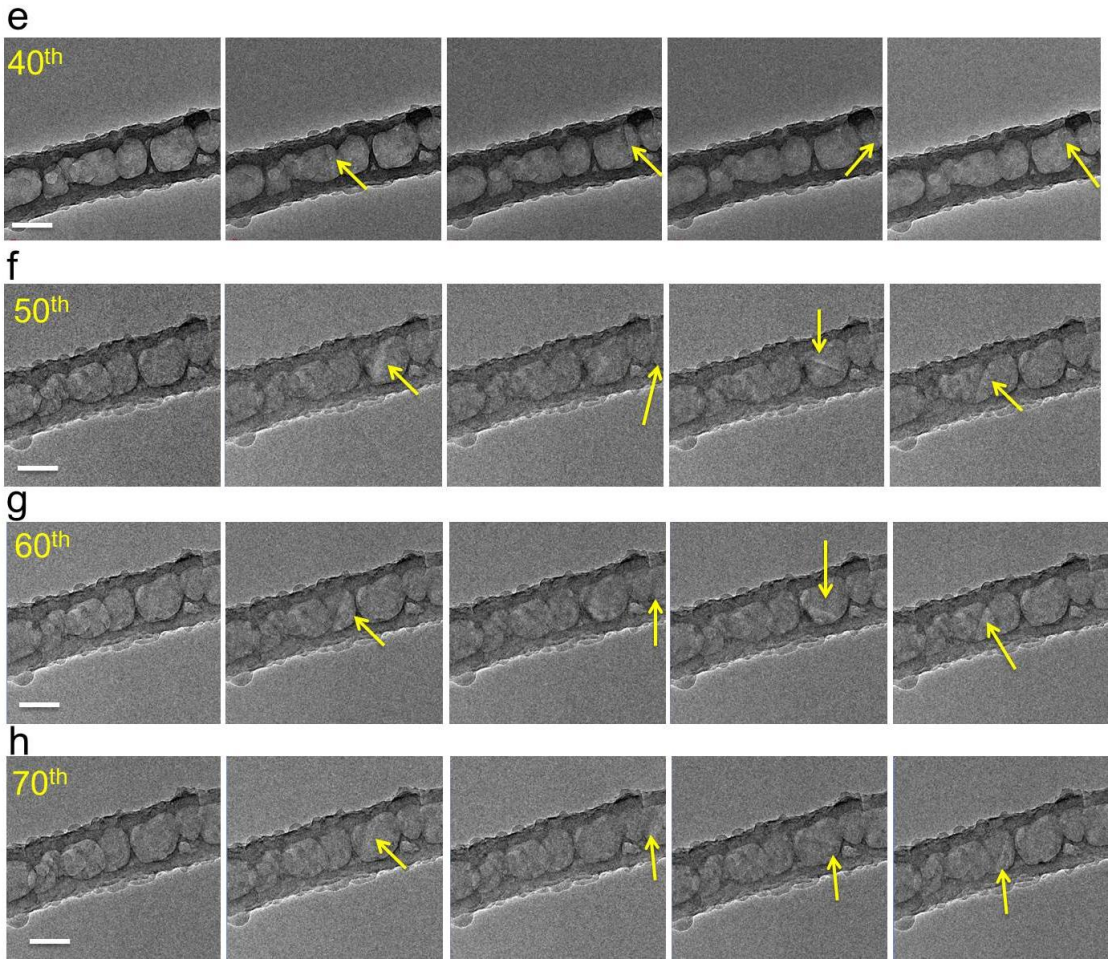
e
40th
f
50th
g
60th
h
70th

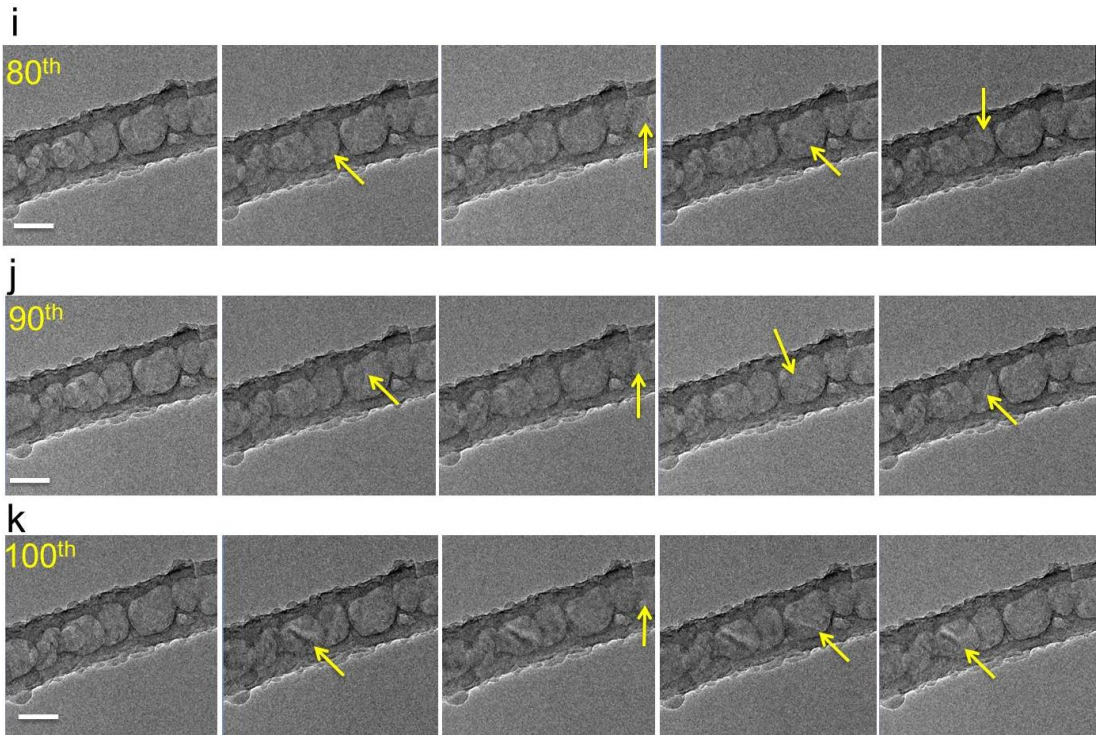

Supplementary Fig. 10 | Li plating/stripping. a-k, 100 cycles of Li plating/stripping in the single carbon tubule. Scale bar, 100 nm. See also Supplementary Video 6. It can be clearly observed that the carbon tubule can maintain the integrity after 100 cycles, and Li can still flow and retract inside the carbon tubule.

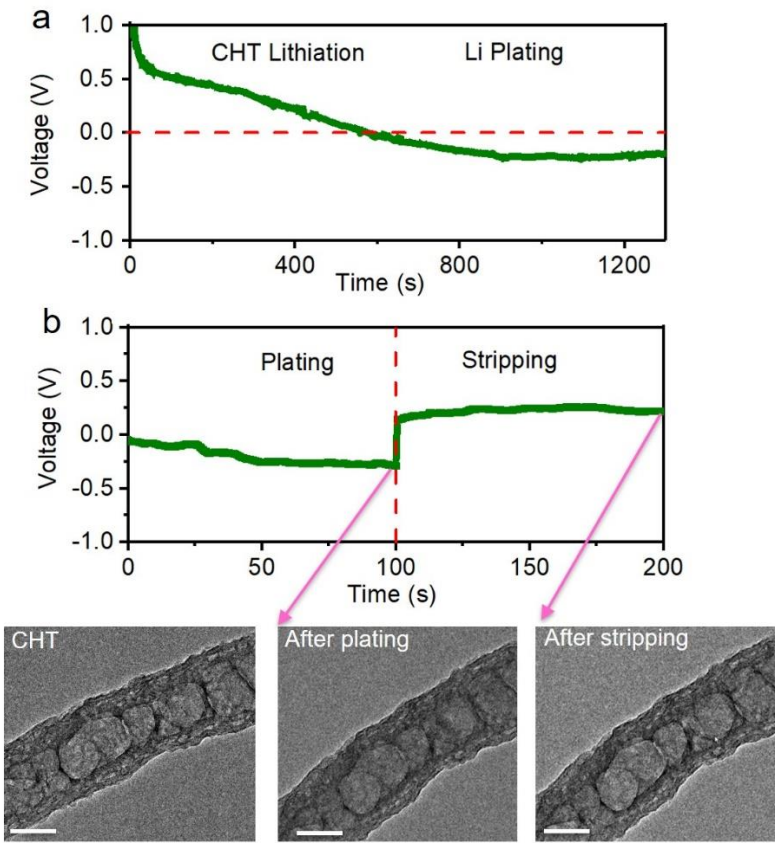

Supplementary Fig. 11 | Charge-discharge profile. **a**, The first charging profile of carbon tubule and **b**, a typical plating/stripping profile. For the first lithiation, it can be seen that above 0V it shows a sloping voltage feature, which can be attributed to the lithiation of the carbon tubule that makes it a MIEC. And below 0V in the same lithiation cycle, we can see a stable voltage plateau, which can be ascribed to Li metal plating inside the carbon tubule. During charging, the Li_{BCC} can be plated inside carbon tubule. During discharging, the Li_{BCC} can be stripped with an overpotential of ~ -0.25V. The carbon tubule with/without Li_{BCC} metal filled inside the channel can be observed correspondingly, as shown from the TEM images indicated from the charge-discharge profile. It can be seen that after plating the TEM image of carbon tubule with Li metal filled inside shows a darker contrast.

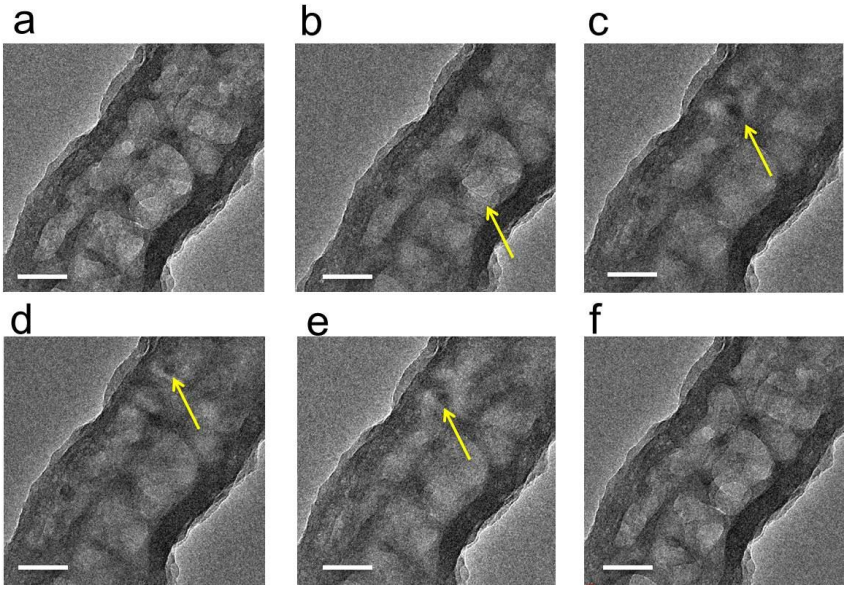

Supplementary Fig. 12 | Li plating/stripping. a-f, TEM imaging of (**a-c**) Li plating and (**d-f**) stripping process in the carbon tubule with inner diameter of ~ 200 nm and wall thickness of 50 nm. Scale bar, 100 nm.

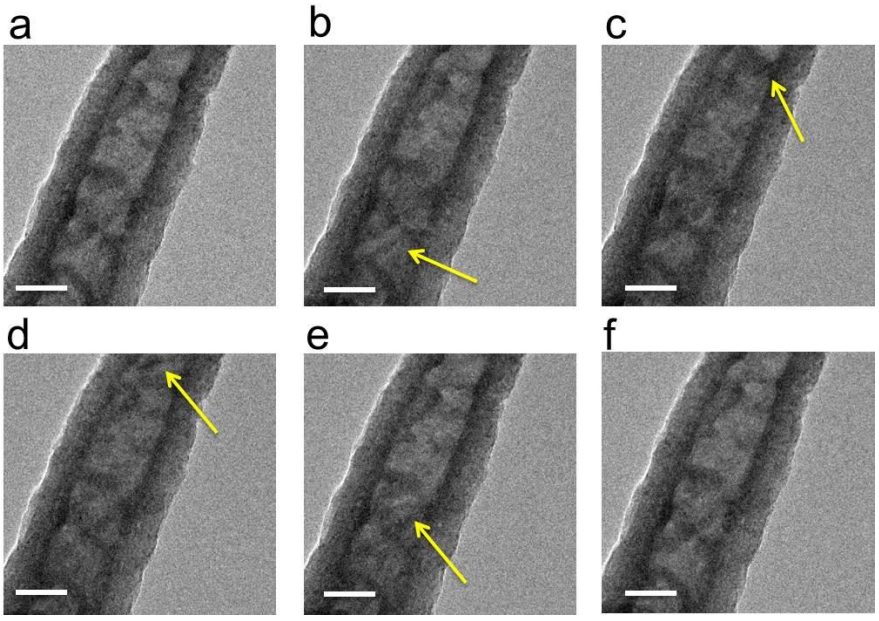

Supplementary Fig. 13 | Li plating/stripping. **a-f**, TEM imaging of (**a-c**) Li plating and (**d-f**) stripping process in the carbon tubule with inner diameter of ~ 100 nm and wall thickness of ~ 60 nm. Scale bar, 100 nm.

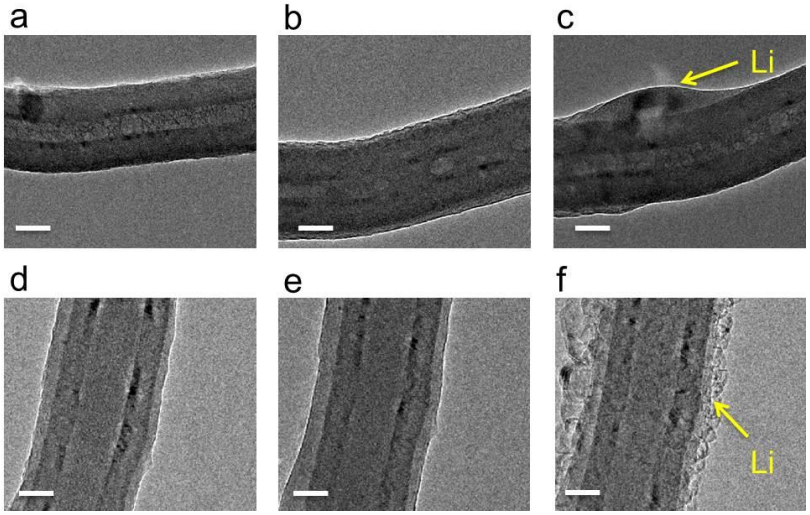

Supplementary Fig. 14 | Li plating/stripping. a-f, TEM imaging of Li plating/stripping in the carbon nanotube with (**a-c**) inner diameter of ~ 30 nm and wall thickness of ~ 50 nm and (**d-f**) the inner diameter of ~ 60 nm and the thickness of ~ 60 nm. Scale bar, 50 nm. Due to the small amount of Li in tube that leads to low contrast variations, the Li plating is not available to be observed. But the plated Li can overflow from the carbon tube as shown in Supplementary Fig. 14 by applying a reverse large bias voltage of 10 V, indicating that Li can also plate/strip inside these small nanotubes.

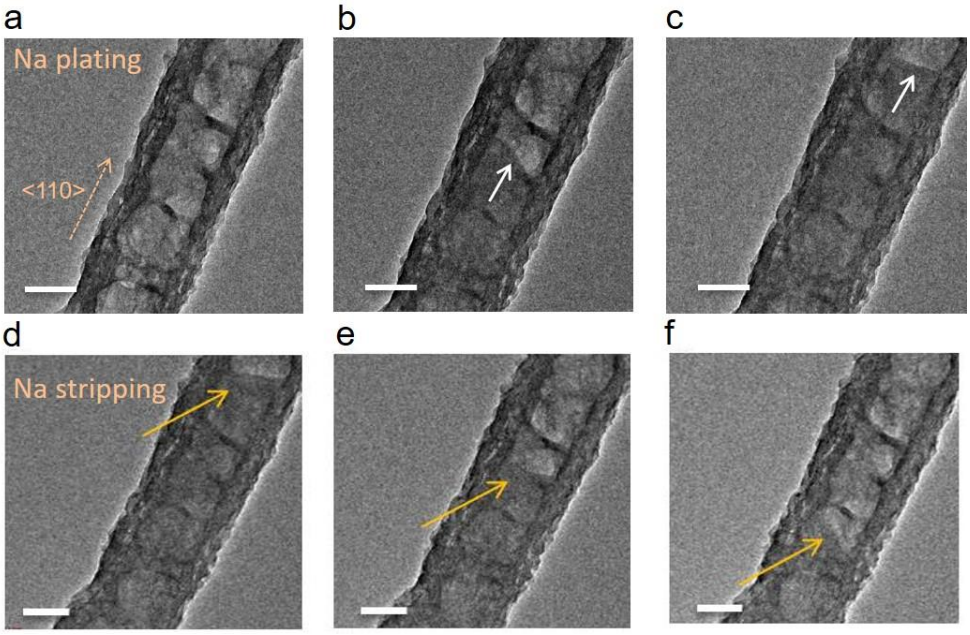

Supplementary Fig. 15 | Na plating/stripping in carbon tubule. a-f, TEM imaging of Na plating/stripping. Scale bar, 100 nm. See also Supplementary Videos 7 and 8.

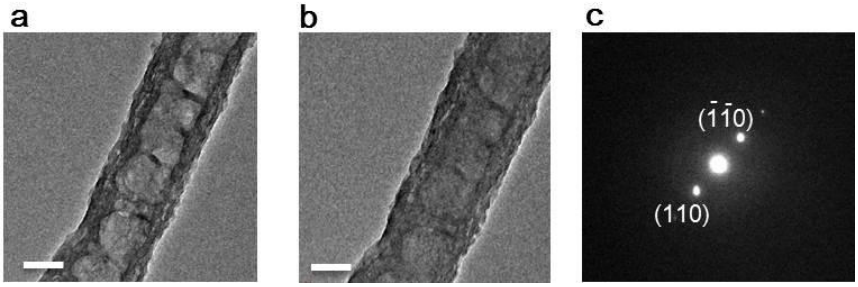

Supplementary Fig. 16 | Na plating in carbon tubule. a, **b**, TEM images of a single carbon tubule before (**a**) and after (**b**) Na plating. **c**, SAED pattern of (**b**), showing that plated Na is single crystal. Scale bar, 100 nm.

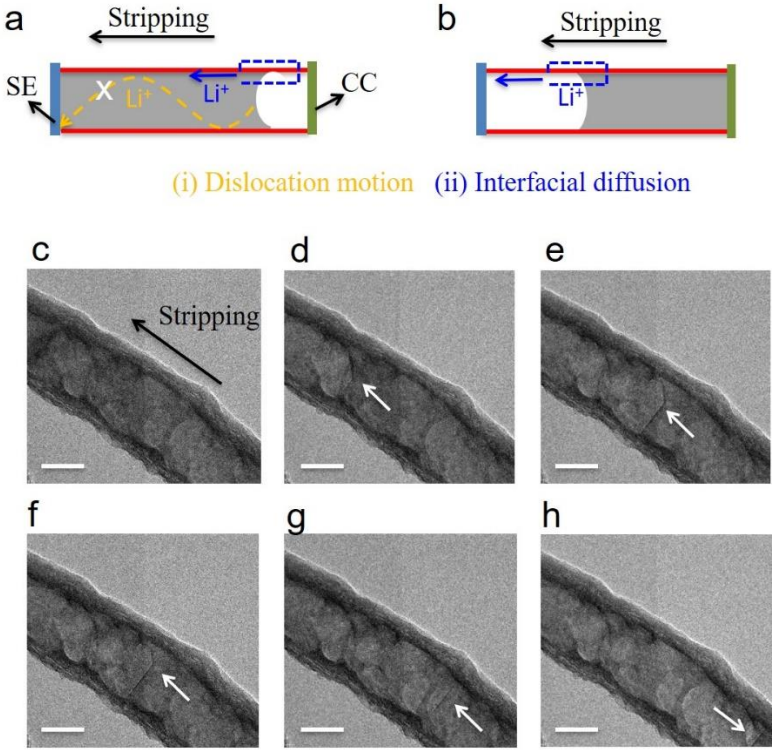

Supplementary Fig. 17 | Demonstration of interfacial diffusion mechanism in Li striping. **a**, **b**, Schematic of Li stripping in carbon tubule (**a**) by a possible combined dislocation motion and interfacial diffusion mechanism and (**b**) by the interfacial diffusion mechanism only, where CC represents current collector and SE stands for solid electrolyte. **c-h**, TEM imaging of Li stripping followed the set-up in (**b**) with a void space between Li metal and the solid electrolyte. Scale bar, 100 nm. See also Supplementary Video 4. We designed and carried on in situ TEM experiment to distinguish between the two possible creep mechanisms (diffusive mechanism or dislocation-slip based convective mechanism). First, we notice that there are differences of the set-ups between Supplementary Fig. 17a and b. In schematic of Supplementary Fig. 17a for stripping of Li_{BCC}, in principle both interfacial diffusion mechanism (noted by blue arrow) and dislocation slip mechanism (noted by yellow arrow) could co-exist, we cannot use in situ TEM experiment to differentiate between the two factors simultaneously. However, in the situation of Supplementary Fig. 17b for the stripping, where there is a void space between the Li metal and the solid electrolyte, matter transport by dislocation-slip mechanism is not possible in the void space on the left, so only interfacial diffusion via MIEC wall interior or interface is possible. We have carried on the in situ TEM experiment that follows the set-up shown in Supplementary Fig. 17b (with a void between Li metal and the solid electrolyte), and it shows in Supplementary Fig. 17c-h that the stripping process can still go smoothly with a stripping rate similar to that of other stripping experiments without the void, showing the mass transport must be through the MIEC wall or interface. The white arrows in Supplementary Fig. 17c-h indicate the movement of the free surface of the Li_{BCC}, as the Li atoms on free surface diffuse to the Li_{BCC}/MIEC interface and undergo interfacial diffusion. This then excludes dislocation-slip based convective mechanism as a major kinetic mechanism, since dislocation slip cannot exist in the void space. Thus interfacial diffusion is proven to be the dominant mechanism which leads to the Li metal deposition and stripping.

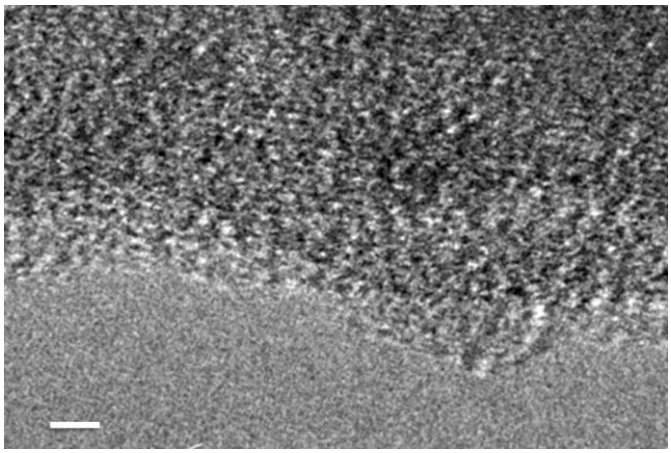

Supplementary Fig. 18 | The outer surface of carbon tubule before Li plating. Scale bar, 2 nm. We cannot find a Li_2O layer on the same outer surface region of carbon tubule as Fig.3a before Li plating.

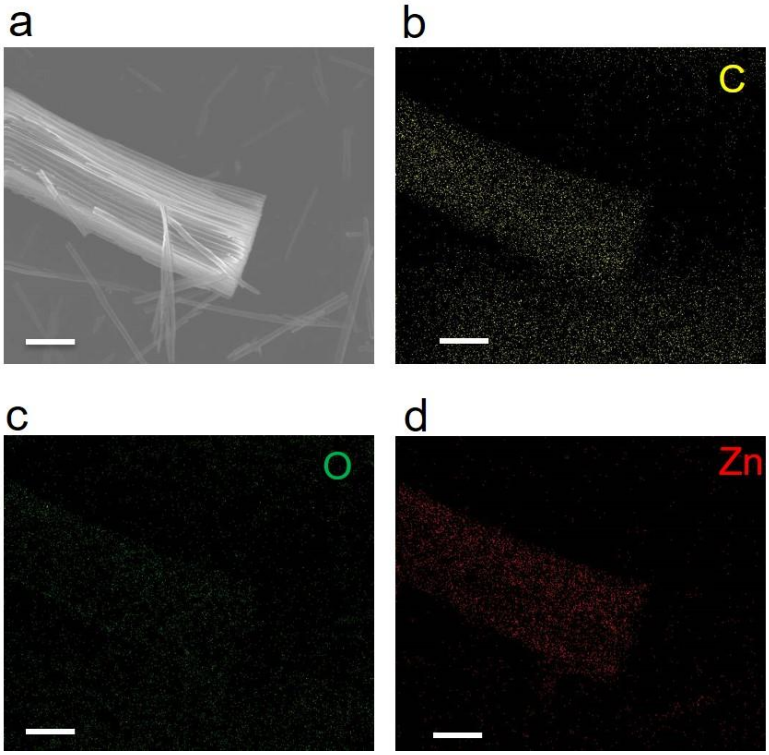

Supplementary Fig. 19 | Morphology of ZnO-coated carbonaceous tubules. a, FESEM image and the EDX mapping of ZnO-coated carbonaceous tubules. Scale bar, **2** μm. EDX mapping shows that ZnO can be deposited into the carbonaceous tubules by atomic layer deposition (ALD).

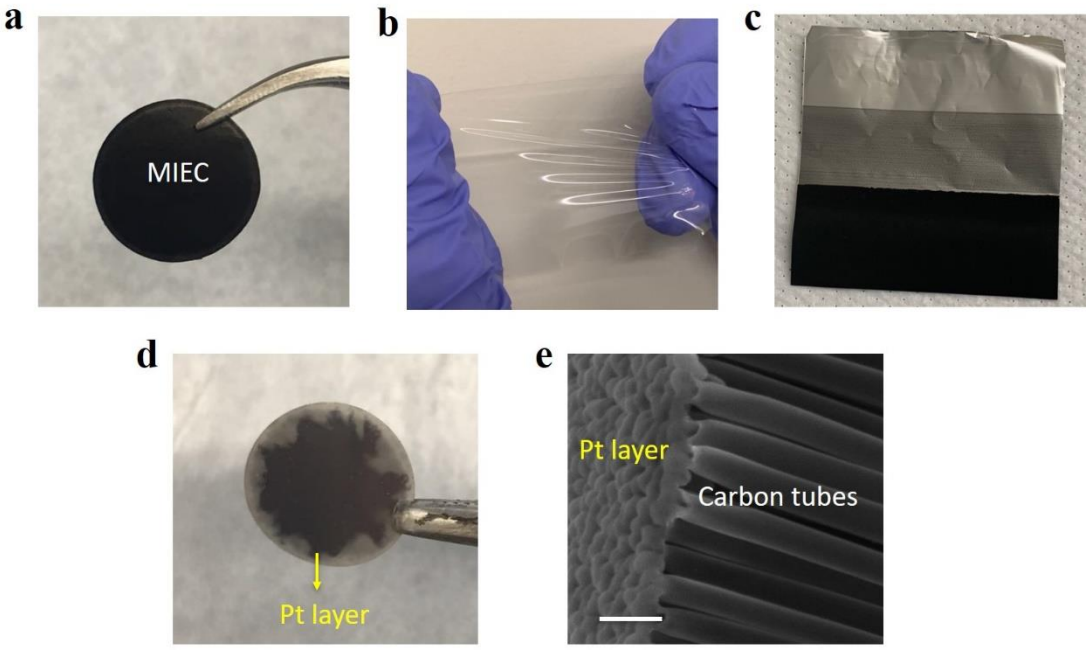

Supplementary Fig. 20 | Photos and FESEM image of the components of the battery. a,d, Photos of the prepared MIEC tubules with Pt layer on bottom, **b**, PEO-based/LiTFSI solid electrolyte film and **c**, $LiFePO_4$ cathode. **e**, FESEM image of aligned carbon tubes bonded to Pt layer. Scale bar, 500 nm.

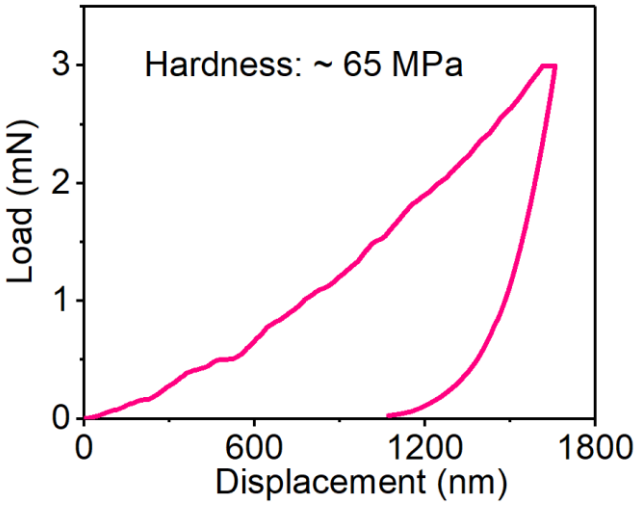

Supplementary Fig. 21 | Nanoindentation. Typical load-displacement curve of the MIEC tubules by nanoindentation.

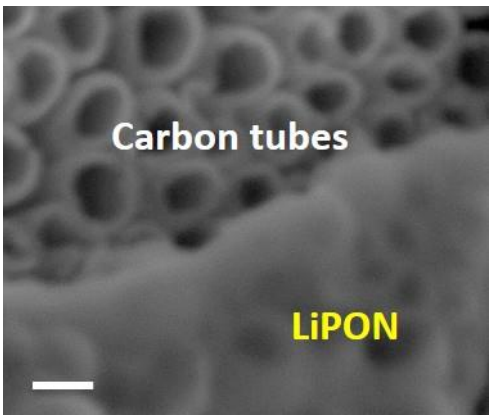

Supplementary Fig. 22 | Morphology. FESEM image of carbonaceous tubules to show that it is well sealed by a layer of LiPON. Scale bar, 200 nm.

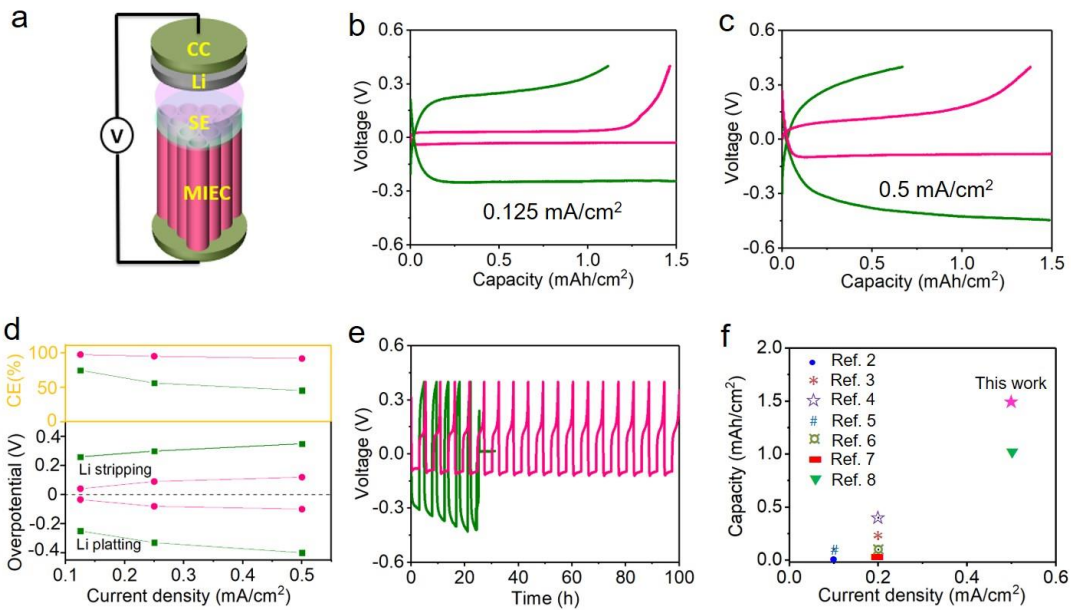

Supplementary Fig. 23 | Electrochemical performance of the half cell. **a**, Schematic of the proposed half cell design. **b,c**, Li plating/stripping profiles, **d**, overpotentials and CEs at different current densities and **e**, charge/discharge voltage profiles of the Li/SE/MIEC half cell. **f**, Comparison of the current density and areal capacity of Li metal anodes in our work and previous reports with all-solid-state electrolyte. The pink color stands for the use of 3D MIEC on the Pt layer as a Li host, while the green color stands for the use of carbon-coated Cu foil as a Li host. Refs.2-8 in Supplementary Fig. 23f can be seen in the 'Reference' section of Supplementary Materials (Page 34).

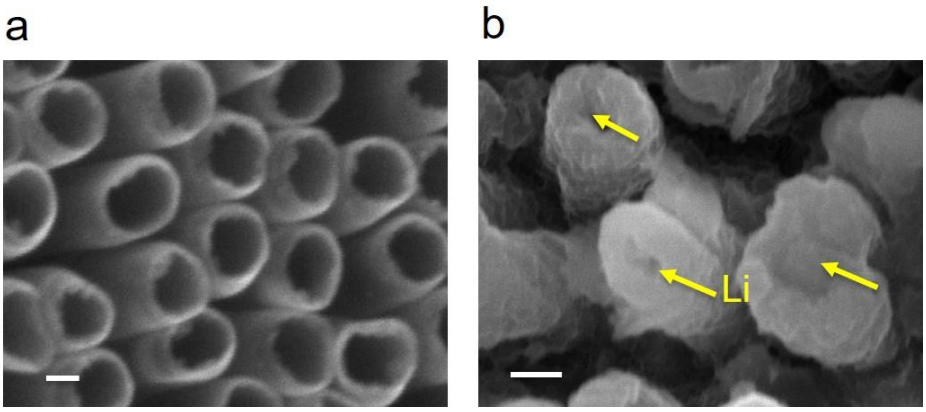

Supplementary Fig. 24 | Li metal deposited in MIEC channel. **a**, **b**, FESEM images of the MIEC channels before (**a**) and after (**b**) Li platting. Scale bar, 100 nm. It is clear that in the actual battery, Li metal is well deposited and filled inside the channels.

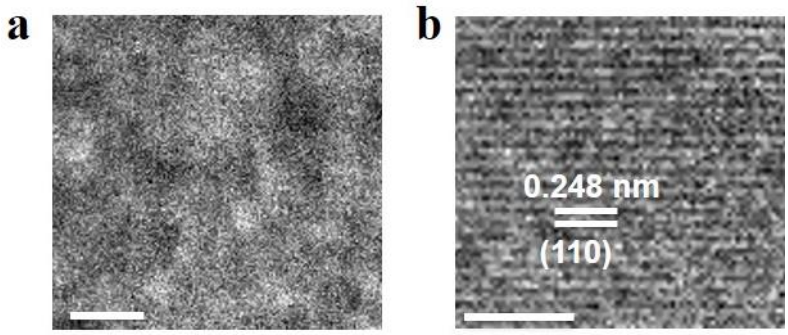

Supplementary Fig. 25 | The effect of carbon tubule encapsulation on imaging the Li crystal. **a**, **b**, HRTEM images of Li (**a**) without and (**b**) with the carbon tubule encapsulation. Scale bar, 2 nm. As shown in Supplementary Fig. 25, if there is no carbon tubule, the Li crystal is very easy to be damaged and amorphized by electron beam, and we cannot see Li_{BCC} lattice. But if Li plates inside the carbon tubule, we can maintain clear Li_{BCC} lattice imaging for several seconds, indicating that the carbon tubule is able to reduce the electron beam damage.

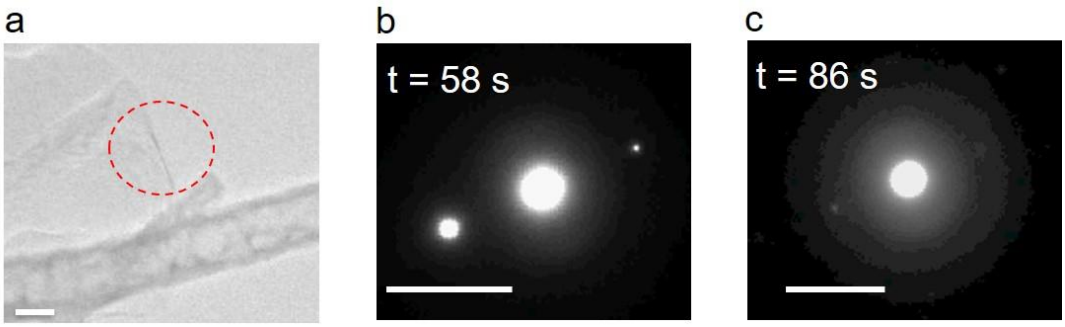

Supplementary Fig. 26 | Stability of Li metal outside carbon tubule under e-beam radiation. **a**, TEM image of Li_{BCC} grown outside carbon tubule and its corresponding SAED patterns (with the selected area aperture labelled by the red dashed circle) under the electron beam current of 3 mA/cm^2: taken with a total radiation time of **b**, t = 58 s and **c**, t = 86 s. Scale bar for **a**, 100 nm. Scale bar for **b**, **c**, 5 nm^{-1}. Clearly, the diffraction spots disappear within ~ 1.5 min, showing an amorphous like ring pattern.

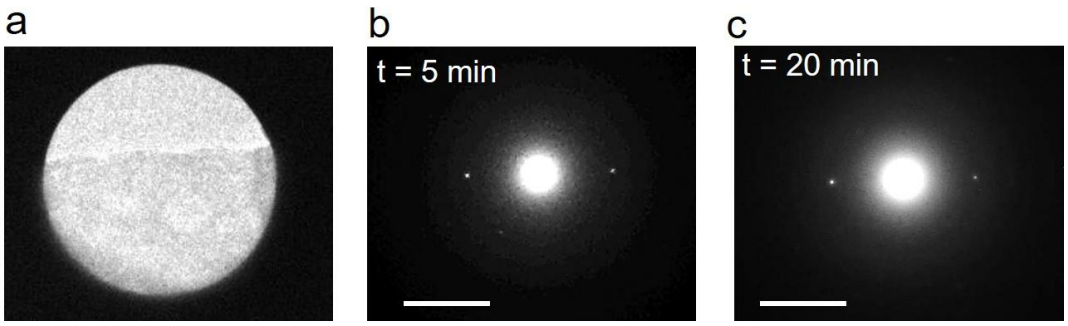

Supplementary Fig. 27 | Stability of Li metal encapsulated by carbon tubule under e-beam radiation. **a**, Li metal inside carbon tubule within the selected-area aperture and its corresponding SAED patterns under an electron beam current of 3 mA/cm^2: taken with a total radiation time of **b**, t = 5 min and **c**, t = 20 min. Scale bar, 5 nm^{-1}. The Li_{BCC} diffraction spots can maintain over 20 min, demonstrating that the carbon tubule encapsulation can significantly reduce the tendency to amorphize.

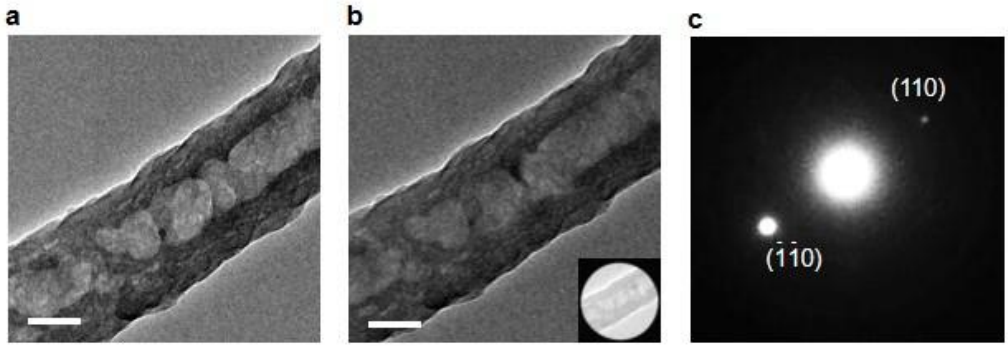

Supplementary Fig. 28 | Li plating without E-beam a, TEM image of carbon tubule taken before Li plating, **c**, SAED pattern taken simultaneously with the opening of the electron beam after plating, and **b**, TEM image of carbon tubule taken after the Li plating. Scale bar, 100nm.

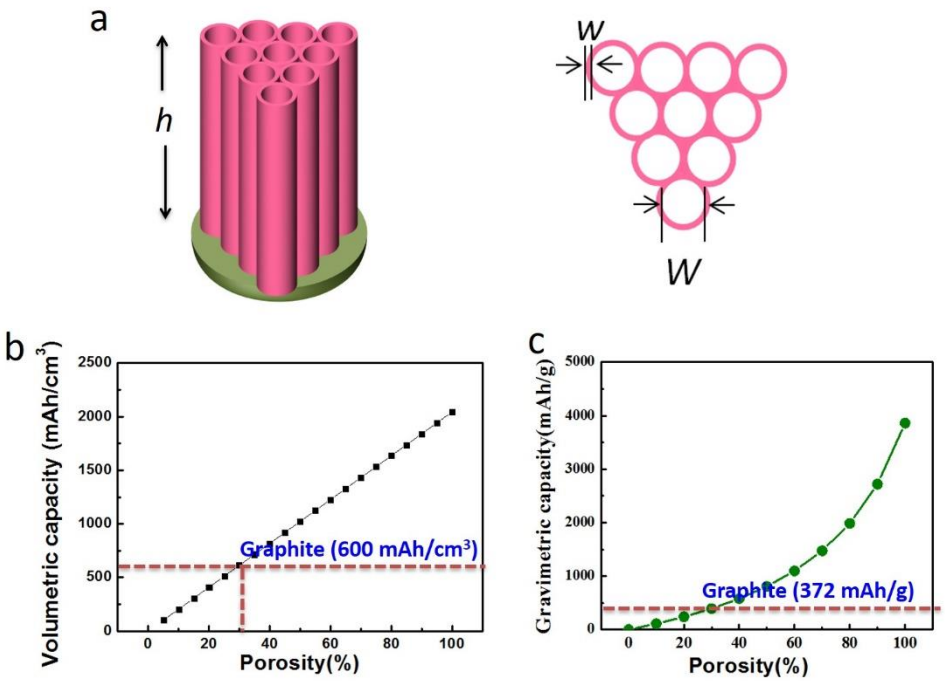

Supplementary Fig. 29 | Calculation of theoretical energy density of Li. a, Geometry of carbonaceous MIEC tubules, **b**, volumetric capacity and, **c**, gravimetric capacity based on the weight of Li and carbonaceous MIEC tubules as a function of porosity.

Supplementary Videos

Supplementary Video 1. An in situ TEM video showing Li plating inside the carbon hollow tubule with ZnO_x (Fig. 2b-d).

Supplementary Video 2. An in situ SAED video showing the changes of SAED on tubule region for the carbon tubular with ZnO_x when Li plating occurs (Fig. 2e,f).

Supplementary Video 3. An in situ TEM video showing the HRTEM imaging of Li plating inside the carbon tubular when the fresh Li crystal first forms inside the field of camera (Fig. 2g-i).

Supplementary Video 4. A speeded-up in situ TEM video showing the Li stripping process inside the carbon tubular when there is a void plug between Li metal and the solid electrolyte (Fig. 2j-l and Supplementary Fig. 17).

Supplementary Video 5. A speeded-up in situ TEM video showing some typical plating/stripping cycles including the 1^{st} and the 30^{th} in the double aligned carbon tubulars (Supplementary Fig. 8).

Supplementary Video 6. A speeded-up in situ TEM video showing Li plating/stripping for 100 cycles in the single carbon tubular (Supplementary Fig. 10).

Supplementary Video 7. A speeded-up in situ TEM video showing Na plating inside the carbon tubular (Supplementary Fig. 15).

Supplementary Video 8. A speeded-up in situ TEM video showing Na striping inside the carbon tubular (Supplementary Fig. 15).

Supplementary Video 9. An in situ TEM video showing the dark-field imaging of the complete wetting of Li, spreading along the tubule outer surface with zero contact angle (Fig. 3b-f).

Reference

1. Yingying, L. *et al.* Application of the soluble salt-assisted route to scalable synthesis of ZnO nanopowder with repeated photocatalytic activity. *Nanotechnology* **23**, 065402 (2012).
2. Wang, C. *et al.* Conformal, Nanoscale ZnO Surface Modification of Garnet-Based Solid-State Electrolyte for Lithium Metal Anodes. *Nano Lett.* **17**, 565-571 (2017).
3. Li, Y. *et al.* Mastering the interface for advanced all-solid-state lithium rechargeable batteries. *Proc. Natl. Acad. Sci.* **113**, 13313-13317 (2016).
4. Sharafi, A. *et al.* Surface Chemistry Mechanism of Ultra-Low Interfacial Resistance in the Solid-State Electrolyte $Li_7La_3Zr_2O_{12}$. *Chem. Mater.* **29**, 7961-7968 (2017).
5. Han, X. *et al.* Negating interfacial impedance in garnet-based solid-state Li metal batteries. *Nat. Mater.* **16**, 572 (2016).
6. Luo, W. *et al.* Transition from Superlithiophobicity to Superlithiophilicity of Garnet Solid-State Electrolyte. *J. Am. Chem. Soc.* **138**, 12258-12262 (2016).
7. Fu, K. *et al.* Toward garnet electrolyte–based Li metal batteries: An ultrathin, highly effective, artificial solid-state electrolyte/metallic Li interface. *Sci. Adv.* **3**, e1601659 (2017).
8. Yang, C. *et al.* Continuous plating/stripping behavior of solid-state lithium metal anode in a 3D ion-conductive framework. *Proc. Natl. Acad. Sci.* **115**, 3770-3775 (2018).